A&A 392, 417–451 (2002)
DOI: 10.1051/0004-6361:20020908

Astronomy & Astrophysics

An all–sky study of compact, isolated high–velocity clouds

V. de Heij[1], R. Braun[2], and W. B. Burton[1,3]

[1] Sterrewacht Leiden, PO Box 9513, 2300 RA Leiden, The Netherlands
[2] Netherlands Foundation for Research in Astronomy, PO Box 2, 7990 AA Dwingeloo, The Netherlands
[3] National Radio Astronomy Observatory, 520 Edgemont Road, Charlottesville, Virginia 22903, USA

Received 25 February 2002 / Accepted 14 June 2002

Abstract. We combine the catalog of compact high–velocity H I clouds extracted by de Heij et al. (2002) from the Leiden/Dwingeloo Survey in the northern hemisphere with the catalog extracted by Putman et al. (2002) from the Parkes HIPASS data in the southern hemisphere, and analyze the all–sky properties of the ensemble. Compact high–velocity clouds are a subclass of the general high–velocity cloud phenomenon which are isolated in position and velocity from the extended high–velocity Complexes and Streams down to column densities below 1.5×10^{18} cm^{-2}. Objects satisfying these criteria for isolation are found to have a median angular size of less than one degree. We discuss selection effects relevant to the two surveys; in particular the crucial role played by obscuration due to Galactic H I. Five principal observables are defined for the CHVC population: (1) the spatial deployment of the objects on the sky, (2) the kinematic distribution, (3) the number distribution of observed H I column densities, (4) the number distribution of angular sizes, and (5) the number distribution of H I linewidth. Two classes of models are considered to reproduce the observed properties. The agreement of models with the data is judged by extracting these same observables from simulations, in a manner consistent with the sensitivities of the observations and explicitly taking account of Galactic obscuration. We show that models in which the CHVCs are the H I counterparts of dark–matter halos evolving in the Local Group potential provide a good match to the observables. The best–fitting populations have a maximum HI mass of 10^7 $M_\odot$, a power-law slope of the HI mass distribution in the range -1.7 to -1.8, and a Gaussian dispersion for their spatial distributions of between 150 and 200 kpc centered on both the Milky Way and M 31. Given its greater mean distance, only a small fraction of the M 31 sub–population is predicted to have been detected in present surveys. An empirical model for an extended Galactic halo distribution for the CHVCs is also considered. While reproducing some aspects of the population, this class of models does not account for some key systematic features of the population.

Key words. ISM: atoms – ISM: clouds – Galaxy: evolution – Galaxy: formation – galaxies: dwarf – galaxies: Local Group

1. Introduction

Since the discovery of the H I high–velocity clouds by Muller et al. (1963), different explanations, each with its own characteristic distance scale, have been proposed. It is likely that not all of the anomalous–velocity H I represents a single phenomenon, in a single physical state. Determining the topology of the entire population of anomalous–velocity H I is not a simple matter, and the task is all the more daunting to carry out on an all–sky basis because of disparities between the observational survey material available from the northern and southern hemispheres. The question of distance remains the most important, because the principal physical parameters depend on distance: mass varying as d^2, density as d^{-1}, and linear size directly as d. Most of the H I emission at anomalous velocities is contributed from extended complexes containing internal sub-structure but embedded in a common diffuse envelope, with angular sizes up to tens of degrees. Such structures include the Magellanic Stream of debris from the Galaxy/LMC interaction and several HVC complexes, most notably complexes A, C, and H. The complexes are few in number but dominate the H I flux observed.

The Magellanic Stream comprises gas stripped from the Large Magellanic Cloud, either by the Galactic tidal field or by the ram–pressure of the motion of the LMC through the gaseous halo of the Galaxy. It therefore will be located at a distance comparable to that of the Magellanic Cloud, i.e. some 50 kpc (see e.g. Putman & Gibson 1999). The distance to Complex A has been constrained by van Woerden et al. (1999) and then more tightly by Wakker (2001) to lie within the distance range $8 < d < 10$ kpc. If, as seems plausible, the other large complexes also lie at distances ranging from several to some 50 kpc, they will have been substantially affected by the radiation and gravitational fields of the Milky Way.

Another category of anomalous H I high–velocity clouds are the compact, isolated high–velocity clouds discussed by Braun & Burton (1999). CHVCs are distinct from the HVC complexes in that they are sharply bounded in angular extent

Send offprint requests to: R. Braun,
e-mail: rbraun@astron.nl

at very low column density limits, i.e. below $1.5{\times}10^{18}\,\mathrm{cm}^{-2}$ (de Heij et al. 2002). This is an order of magnitude lower than the critical H I column density of about $2{\times}10^{19}\,\mathrm{cm}^{-2}$, where the ionized fraction is thought to increase dramatically due to the extragalactic radiation field. For this reason, these objects are likely to provide their own shielding to ionizing radiation. Although not selected on the basis of angular size, such sharply bounded objects are found to be rather compact, with a median angular size of less than 1 degree.

An analogy of the CHVC ensemble with that of the dwarf galaxy population in the Local Group is suggestive, and illustrates the hypothesis that is under discussion here. Some few Local Group dwarf galaxies also extend over large angles. The Sgr Dwarf Spheroidal discovered by Ibata et al. (1994) spans some 40°; presumably it was once a rather conventional dwarf, but its current proximity to the Milky Way accounts for its large angular size. This proximity has fundamentally distorted its shape, and will determine its further evolution. The streams of stars found in the halo of the Galaxy by Helmi et al. (1999) probably represent even more dramatic examples of the fate which awaits dwarf galaxies which transgress into the sphere of the Galaxy's dominance. Analogous stellar streams have been found in M 31 by Ibata et al. (2001) and by Choi et al. (2002), as well as in association with Local Group dwarf galaxies by Majewski et al. (2000), indicating that accretion (and subsequent stripping) of satellites is an ongoing process. If a selection were to be made of the dwarf galaxy population in the Local Group on the basis of angular size, the few large–angle systems which would be selected, namely the LMC and SMC, and the Sgr dwarf, and – depending on the flexibility of the selection criteria – perhaps the ill–fated coherent stellar streams in the Galactic halo, would represent systems nearby, of large angular extent, and currently undergoing substantial evolution. Those systems selected on the basis of being compact and isolated, on the other hand, would represent dwarf galaxies typically at substantial distances and typically at a more primitive stage in their evolution. Regarding distance and evolutionary status they would differ from the nearby, extended objects, although at some earlier stage the distinction would not have been relevant.

The possibility that some of the high–velocity clouds might be essentially extragalactic has been considered in various contexts by, among others, Oort (1966, 1970, 1981), Verschuur (1975), Eichler (1976), Einasto et al. (1976), Giovanelli (1981), Bajaja et al. (1987), Wakker & van Woerden (1997), Braun & Burton (1999), and Blitz et al. (1999). It is interesting to note that the principal earlier arguments given against a Local Group deployment, most effectively in the papers cited above by Oort and Giovanelli, were based on the angular sizes of the few large complexes and on the predominance of negative velocities in the single hemisphere of the sky for which substantial observational data were then available. The more complete data available now, however, show about as many features at positive velocities as at negative ones. It is also interesting to note that the papers by Eichler and by Einasto et al. cited above consider distant high–velocity clouds as possible sources of matter, including dark matter, fueling continuing evolution of the Galaxy. Blitz et al. (1999) revived the suggestion that high–velocity clouds are the primordial building blocks fueling galactic growth and evolution, and argued that the extended complexes owe their angular extent to their proximity.

Braun & Burton (1999) identified CHVCs as a subset of the anomalous–velocity gas that might be characteristic of a single class of HVCs, whose members plausibly originated under common circumstances and share a common subsequent evolutionary history. They emphasized the importance of extracting a homogenous sample of independently confirmed objects from well–sampled, high–sensitivity H I surveys. The spatial and kinematic distributions of the CHVCs were found by Braun & Burton to be consistent with a dynamically cold ensemble spread throughout the Local Group, but with a net negative velocity with respect to the mean of the Local Group galaxies. They suggested that the CHVCs might represent the low–circular–velocity dark matter halos predicted by Klypin et al. (1999) and Moore et al. (1999) in the context of the hierarchical structure paradigm of galactic evolution. These halos would contain no, or only a few, stars; most of their visible matter would be in the form of atomic hydrogen. Although many of the halos would already have been accreted into the Galaxy or M 31, some would still populate the Local Group, either located in the far field or concentrated around the two dominate Local Group galaxies. Those passing close to either the Milky Way or M 31 would be ram–pressure stripped of their gas and tidally disrupted by the gravitational field. Near the Milky Way, the tidally distorted features would correspond to the high–velocity–cloud complexes observed.

The quality and quantity of survey material is important to interpretation of the CHVC population, which is a global one. The observational data entering this analysis involved merging two catalogs of CHVCs, one based on the material in the Leiden/Dwingeloo Survey (LDS) of Hartmann & Burton (1997), and the other based on the H I Parkes All–Sky Survey (HIPASS) described by Barnes et al. (2001). Both of these surveys were searched for anomalous–velocity features using the algorithm described by de Heij et al. (2002, Paper I). This algorithm led to the LDS catalog of de Heij et al. for the CHVCs at declinations north of −30°, and to the HIPASS catalog of Putman et al. (2002) for those at $\delta < 0°$. The surveys overlap in the declination range $+2° < \delta < -30°$, allowing estimates of the relative completeness of the catalogs. We are able to predict how a survey with the LDS parameters would respond to the CHVCs detected by HIPASS, and vice versa. In the subsequent simulations, we are able to *sample the simulated material as if it were being observed* by one of these surveys.

This paper is organized as follows. We describe the application of the algorithm in Sect. 2.1. In Sect. 2.2 we discuss various observational selection effects, and indicate how to account for these. We address obscuration by our own Galaxy in Sect. 2.2.1, the consequences of the differing observational parameters of the LDS and HIPASS data in Sect. 2.2.2, and the resulting differing degrees of completeness of the LDS and HIPASS catalogs in Sect. 2.2.3. We discuss the observable all–sky properties of the CHVC ensemble in Sect. 3, including the spatial deployment (in Sect. 3.1), the kinematic deployment (in Sect. 3.2), and the distributions of H I flux and angular size (in Sect. 3.3). We then attempt to reproduce these properties

by considering models, first based on Local Group distributions as discussed in Sect. 4 and then on distributions within an extended Galactic Halo as discussed in Sect. 5; these simulations are sampled *as if being observed* with the LDS and HIPASS programs. We discuss the conclusions that can be drawn from this analysis in Sect. 6.

2. Observations representing CHVCs over the entire sky

2.1. Identification criteria

A full description of the cloud extraction algorithm is given in Paper I; the most salient aspects of the algorithm are the following:

- All pixels in the HIPASS and LDS material above the 1.5σ level (as appropriate to the particular survey) were assigned to a local intensity maximum; each pixel was assigned to the same maximum as its brightest neighboring pixel. If the local maximum was brighter than 3 σ, then the local maximum and the pixels which were assigned to it were considered to constitute a cloudlet;
- Adjacent cloudlets were merged into clouds if the brightest enclosing contour for the two cloudlets either exceeds 40% of the brighter peak or if the brightness exceeds 10σ;
- Those merged cloudlets for which the peak temperature exceeds 5 σ were deemed clouds, and were entered in the catalog pending further consideration of their deviation velocity, as described below. The value of the noise that was used for this selection was determined locally, whereas for the other steps a preset noise value was used.

To minimize the influence of noise on the peak detection, the data were first smoothed along both the spatial and spectral axes. The rms fluctation level noted above refers to that within the smoothed data. Once the relevant pixels were assigned to a cloud, unsmoothed data were used to determine the cloud properties.

The Paper I search algorithm led to the identification of sub–structure within extended anomalous–velocity cloud complexes as well as to the identification of sharply bounded, isolated sources. Because of the importance to the present analysis of selecting only isolated objects, we comment on the determination of the degree of isolation. In order to determine the degree of isolation of the clouds that were found by the algorithm, velocity–integrated images were constructed of 10° by 10° fields centered on each general catalog entry. The range of integration in these moment maps extended over the velocities of all of the pixels that were assigned to a particular cloud. The CHVC classification then depended on the column density distribution at the lowest significant contour level (about 3σ) of 1.5×10^{18} cm^{-2}. We demanded that this contour satisfy the following criteria: (1) that it be closed, with its greatest radial extent less than the 10° by 10° image size; and (2) that it not be elongated in the direction of any nearby extended emission. Since some subjectivity was involved in this assessment, two of the authors (VdH and RB) each independently carried out a complete classification of all sources in the HIPASS and LDS catalogs. Identical classification was given to about 95% of the sample, and consensus was reached on the remaining 5% after re–examination.

A slightly different criterion for isolation was employed by Putman et al. (2002) in their analysis of the HIPASS sample of HVCs. Rather than employing the column density contour at a fixed minimum value to make this assessment, they employed the contour at 25% of the peak $N_{\rm HI}$ for each object. Since the majority of detected objects are relatively faint, with a peak column density near 12σ, the two criteria are nearly identical for most objects. Only for the brightest ∼10% of sources might the resulting classifications differ. We have reclassified the entire HIPASS HVC catalog with the absolute $N_{\rm HI}$ criteria above, and have determined identical classifications for 1800 of the 1997 objects listed. Given that the agreement in classification is better than 90%, we have chosen to simply employ the Putman et al. classifications in the current study. In this way the analysis presented here can be reproduced from these published sources.

High–velocity clouds are recognized as such by virtue of their anomalous velocities. Although essentially any physical model of these objects would predict that they also occur at the modest velocities characteristic of the conventional gaseous disk of the Milky Way, at such velocities the objects would not satisfy our criterion for isolation. In our analysis, only anomalous–velocity objects with a deviation velocity greater than 70 km s^{-1} were considered. As defined by Wakker (1990), the deviation velocity is the smallest difference between the velocity of the cloud and any Galactic velocity, measured in the Local Standard of Rest reference frame, allowed by a conventional kinematic model in the same direction. The kinematic and spatial properties of the conventional Galactic HI were described by a thin gaseous disk whose properties of volume density, vertical scale–height, kinetic temperature, and velocity dispersion, remain constant within the solar radius; at larger galactocentric distances the gaseous disk flares and warps, as described in Paper I, following Voskes & Burton (1999). The gas exhibits circular rotation with a flat rotation curve constant at 220 km s^{-1}. Synthetic H I spectra were calculated for this model Galaxy, and then deviation velocities were measured from the extreme–velocity pixels in these spectra for which the intensity exceeded 0.5 K. Selection against objects at $V_{\rm dev} < 70$ km s^{-1} in the LSR frame introduces systematic effects, as discussed in the following subsection.

Although compactness was not explicitly demanded of these isolated objects, the 67 CHVCs found in the LDS survey and the 179 CHVCs found in the HIPASS data have a small median angular size, amounting to less than 1° *FWHM*.

2.2. Selection effects and completeness

The CHVC samples used in this analysis were not extracted from a single, homogeneous set of data, nor are they free of selection effects, nor are they complete. We discuss below how we attempt to recognize and, insofar as possible, to account for some inevitable limitations.

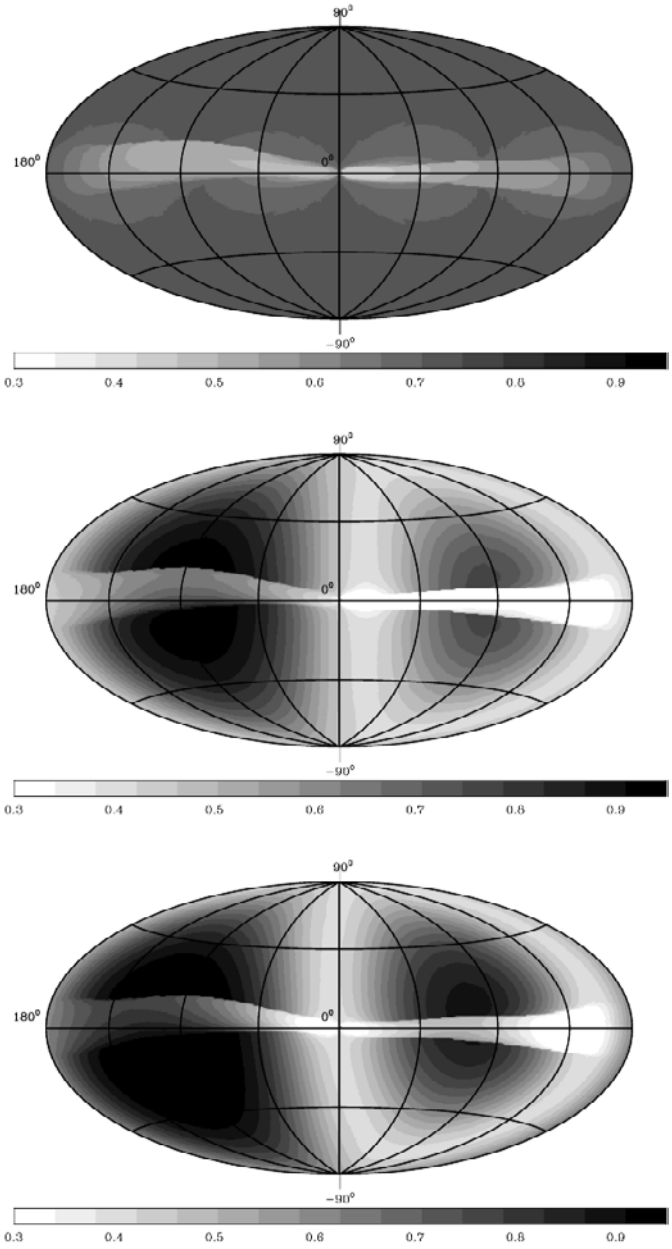

Fig. 1. Fraction of a homogeneously distributed sample of test clouds that is not blended with Galactic emission. The sample was distributed on the sky with a Gaussian velocity distribution in the Local Standard of Rest system (upper panel), the Galactic Standard of Rest system (middle), and the Local Group Standard of Rest (lower). The average velocity of the Gaussian velocity distributions is −50 km s^{-1} for each of the simulations; the velocity dispersion is 240 km s^{-1} for the LSR representation, and 110 km s^{-1} for the GSR and LGSR ones, in rough accordance with the observed situation. The obscuration by Galactic emission was simulated by removing that part of the sample for which the deviation velocity (measured with respect to the LSR) is less than 70 km s^{-1}, based on a model of Galactic kinematics which incorporates observed properties of the gaseous disk, including its warp and flare. The apparent structures are a consequence of the non–uniform obscuration in position and velocity. The appearance of the H I Zone of Avoidance differs when material is considered in different reference frames.

2.2.1. Systematic consequences of obscuration by H I in the Milky Way

The inevitable obscuration that follows from our perspective immersed in the gaseous disk of the Milky Way, and which motivates the use of the deviation velocity, will discriminate against some CHVC detections. We may extend an analogy of the optical Zone of Avoidance to the 21–cm regime. The optical Zone of Avoidance refers to extinction of light by dust in the Milky Way, and thus traces a band with irregular borders but roughly defined by $|b| < 5°$; kinematics are irrelevant in the optical case, since the absorption is broad–band. The HI searches for galaxies in the optical Zone of Avoidance carried out by, among others, Henning et al. (1998) in the north, and by Henning et al. (2000) and Juraszek (2000) in the south, were confined to $|b| < 5°$.

In the 21–cm regime, extinction due to high–optical–depth foreground H I is largely negligible, but confusion due to line blending occurs at all latitudes. The analogous H I zone refers to a certain range in velocity, of varying width depending on l and on b, but present to some extent everywhere: near zero LSR velocity, the "H I Zone of Avoidance" covers the entire sky. The nearby LSB galaxy Cep I was discovered during CHVC work (Burton et al. 1999); although it is at a relatively substantial latitude, $b = 8\overset{\circ}{.}0$, its velocity of $V_{\rm hel} = 58$ km s^{-1} locates it within the H I obscuration zone. Because of the strong dependence on velocities measured with respect to the Local Standard of Rest, the zone of obscuration is distorted upon transformation to a different kinematic reference frame. (We note that the Magellanic Stream and the HVC complexes plausibly also discriminate against CHVC detections, but because these extended features are smaller in scale and more confined

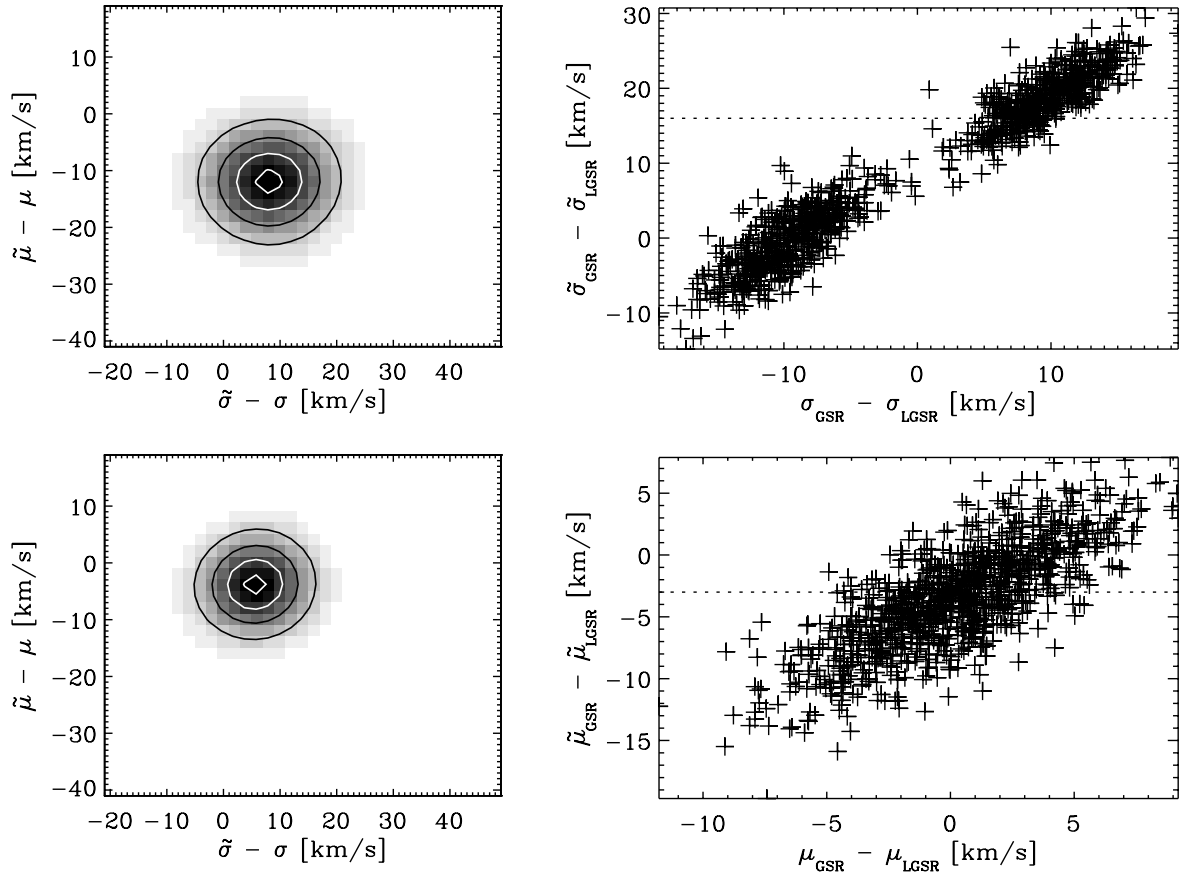

Fig. 2. Demonstration of the influence of Galactic obscuration on observable properties of a CHVC population. The left–hand panels show the distributions of measured (after obscuration) versus actual mean velocity and velocity dispersion determined from a series of 1000 simulations of a population of 200 objects. The upper panel on the left represents a population with a Gaussian velocity distribution in the GSR reference frame, with $\mu = -50$ km s^{-1} and $\sigma = 115$ km s^{-1}; the lower left–hand panel represents a population with a Gaussian velocity distribution in the LGSR frame, with $\mu = -55$ km s^{-1} and $\sigma = 105$ km s^{-1}. Obscuration removes about 30% of the population and leads to both an overestimate of the dispersion and a more negative estimate of the mean velocity. The right–hand panels illustrate the degree to which populations in the GSR and LGSR frames could be distinguished via their statistical parameters. Measured and actual parameter differences between the GSR and LGSR frames are contrasted for 1000 simulated populations of 200 objects, half defined in the GSR frame and half in the LGSR frame. All populations have a mean velocity of −50 km s^{-1} and a dispersion of 110 km s^{-1} in their reference frame. The measured parameter differences for the observed CHVC sample are indicated by the dashed lines. While the mean velocity does not provide significant distinguishing capability between the GSR and LGSR frames, the velocity dispersion does.

in velocity than the Galaxy, we do not consider them further here.)

The relationship between the different velocity reference systems used to characterize the CHVC kinematics is given by the equations below.

$$v_{\rm LSR} = v_{\rm HEL} + 9\cos(l)\cos(b) + 12\sin(l)\cos(b) + 7\sin(b) \quad (1)$$

$$v_{\rm GSR} = v_{\rm LSR} + 0\cos(l)\cos(b) + 220\sin(l)\cos(b) + 0\sin(b) \quad (2)$$

$$v_{\rm LGSR} = v_{\rm GSR} - 62\cos(l)\cos(b) + 40\sin(l)\cos(b) - 35\sin(b). \quad (3)$$

Note that a typographical error is present (the sign of the coefficient of $\sin(b)$) in the version of Eq. (1) that is published in Braun & Burton (1999).

The influence of the obscuration by the modeled Galaxy is illustrated by Fig. 1, where the integral $\int \exp(-(V - \mu)^2/2\sigma^2)dV$ is plotted. The range of integration extends over all velocities which deviate more than 70 km s^{-1} from any Local Standard of Rest (LSR) velocity allowed by the Galactic model described above; μ is the average velocity and σ is the standard deviation of the test clouds. The panels in Fig. 1 show the fraction of a population of clouds, homogeneously distributed on the sky and with a Gaussian velocity distribution relative to a particular reference frame, that are not obscured by virtue of being coincident with H I emission from the Milky Way. The upper panel of the figure represents a model in which the Gaussian velocity distribution is with respect to the Local Standard of Rest frame, with an average velocity of −50 km s^{-1} and dispersion of 240 km s^{-1}, in rough agreement with the measured CHVC values in this frame. In this case the obscuration is simply proportional to the velocity width of the obscuring emission. The obscuration at high latitudes is quite uniform since the infalling population is always displaced from $V_{\rm LSR} = 0$ km s^{-1}, where the obscuring gas resides. The middle panel presents a model wherein the Gaussian velocity distribution is with respect to the Galactic Standard of Rest (GSR)

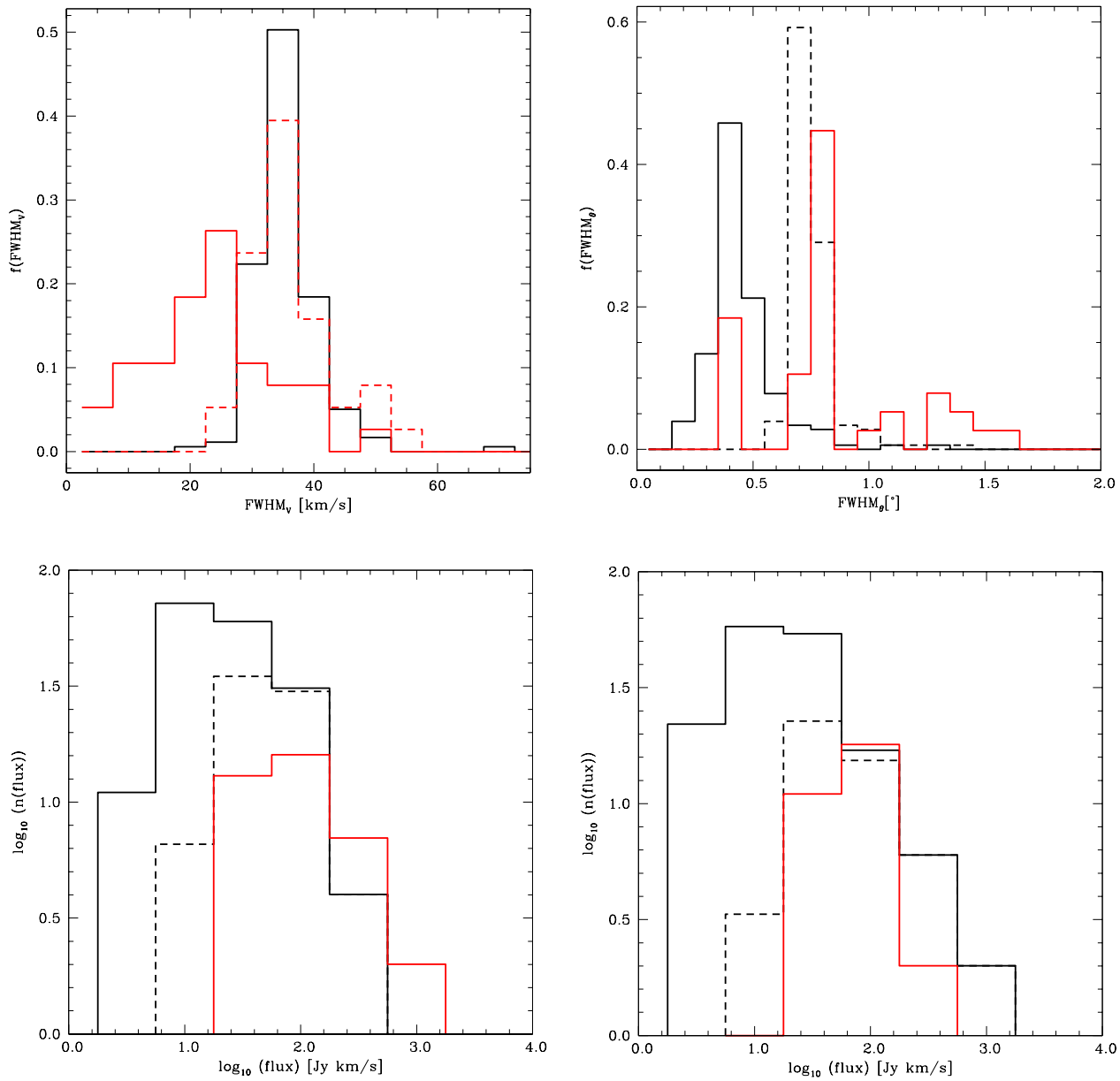

Fig. 3. Demonstration of the effects of differing resolution and sensitivity in the LDS and HIPASS data on the extracted CHVC samples. *Upper left:* comparison of the velocity *FWHM* for the CHVCs found in the HIPASS catalog (black line) with the velocity widths of those found in the LDS catalog (red line). The velocity resolution of the LDS is 1.03 km s^{-1}, but 26 km s^{-1} for HIPASS; after degrading the LDS data to the HIPASS velocity resolution, the dashed red line is obtained. *Upper right:* comparison of the angular *FWHM* for the CHVCs in the HIPASS catalog (black line) with those in the LDS catalog (red line). The angular resolution of the LDS is 36′, but 15′ for HIPASS; the dashed black line shows the HIPASS values after convolving with the LDS beam. *Lower left:* comparison of the total flux of CHVCs found in the HIPASS catalog (black line) with those in the LDS catalog (red line). After compensating the HIPASS detection rates for the lower LDS sensitivity, the dashed black histogram is obtained. The compensation was performed using the relative detection rates in the region of survey overlap (see Fig. 4). *Lower right:* comparison of the total fluxes for the semi–isolated objects (CHVC:s and CHVC?s) entered in the HIPASS catalog (black line) with those in the LDS listing (red line). Compensation of the HIPASS detections to the corresponding LDS sensitivity gives the dashed black line. (This figure is available in color in electronic form.)

frame with an average velocity of −50 km s^{-1} and dispersion of 110 km s^{-1}, in rough agreement with the CHVC values in this frame. The low–latitude obscuration is similar to that in the LSR model, although more strongly modulated since the velocity dispersion is smaller. The high–latitude obscuration is quite strongly modulated since the infall velocity in the GSR frame overlaps with $V_{\rm LSR}$ = 0 km s^{-1} in the plane approximately perpendicular to the direction of rotation, $(l, b) = (90°, 0°)$. Broad apparent maxima in unobscured object density are centered near $l = 90°$ and $l = 270°$. The lower panel presents a model in which the Gaussian velocity distribution is with respect to the Local Group Standard of Rest (LGSR), again

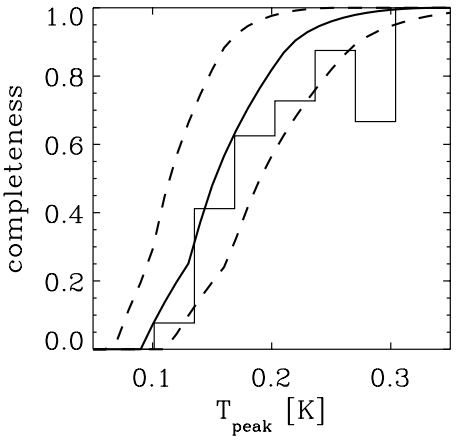

Fig. 4. Indication of the degree of completeness of the CHVC catalog extracted from the LDS by de Heij et al. (2002). The solid curve shows the fraction of external galaxies with the indicated peak H I brightness temperatures that were shown by Hartmann & Burton (1997) to have been detected in the LDS. Dashed lines show the expected completeness for sensitivities that are 25% better or worse, respectively, than that of the LDS. The histogram indicates the fraction of HIPASS sources from the catalog of Putman et al. (2002) within each temperature range that are also found in the LDS, in the declination zone $-30° < \delta < 0°$ where the two surveys overlap.

using an average velocity of −50 km s^{-1} and dispersion of 110 km s^{-1}. The pattern of obscuration is very similar to that of the GSR case, although the maxima in unobscured object density are slightly shifted with respect to $b = 0°$. These results indicate that caution must be exercised in interpreting apparent spatial concentrations of detected objects without properly accounting for the distortions introduced by the H I Zone of Avoidance.

We have also considered how the measured statistics of a distribution, namely the mean velocity and dispersion, are influenced by the non–completeness caused by obscuration. Figure 2 shows the distribution of the errors in the average velocity and dispersions for 1000 simulations, each involving 200 test clouds; one set of simulations was run with the GSR as the natural reference frame, and a second set was run with the LGSR as the natural frame. After removing the test clouds that have an LSR deviation velocity less than 70 km s^{-1}, the velocity dispersion of the simulated ensemble was measured for both the GSR and the LGSR velocity systems, and compared with what would have been determined if there had been no obscuration by the Galaxy.

The upper left–hand panel in Fig. 2 refers to test objects with a Gaussian distribution in $V_{\rm GSR}$ with a dispersion of 115 km s^{-1} and average of −50 km s^{-1}. The measured dispersion exceeds the true one by 9 km s^{-1}, whereas a more negative average velocity is inferred by 12 km s^{-1}. The lower left–hand panel is based upon test samples with a Gaussian distribution in $V_{\rm LGSR}$ with a dispersion of 105 km s^{-1} and an average of −55 km s^{-1}. The differences between the measured and true dispersion and average velocity, of 6 km s^{-1} and −5 km s^{-1}, respectively, are smaller than for the GSR system. From the 200 clouds which were in the input ensemble, an average of 80 were removed because of obscuration in the GSR model and only 60 in the LGSR model, indicating that the statistical properties of the LGSR model are somewhat better preserved in this case. The particular population attributes chosen above for the GSR and LGSR systems were chosen to match the observed parameters in these systems, as shown below in Sect. 3.

Another question that can be addressed with these simulations is whether it might be possible to distinguish between a GSR and an LGSR CHVC population based on a significant difference in the statistical properties. We assessed this by taking 500 populations of 200 objects in both the GSR and LGSR frames, each with a dispersion of 110 km s^{-1} and an average velocity of −50 km s^{-1}. Each of these 1000 populations was analyzed in both the GSR and LGSR frames, both before and after decimation by obscuration. The results are shown in the right–hand panels of Fig. 2 for differences in velocity dispersion (relative to the GSR versus LGSR frames) and mean velocity, respectively. The measured differences in velocity dispersion and mean velocity of our CHVC sample (from Sect. 3) are plotted in these panels as dashed lines. The model results for mean velocity differences form a continuous cloud, for which it is impossible to distinguish between the actual reference frame of the model population. The model results for velocity dispersion differences, on the other hand, are separated into two distinct clouds. The velocity dispersion of each model population is minimized in its own reference frame with a variance of only a few km s^{-1}, while the dispersions within the GSR and LGSR frames are separated by about 20 km s^{-1}, both before and after obscuration. The measured difference in velocity dispersion of the CHVC sample relative to the GSR and LGSR frames, of 16 km s^{-1}, is more consistent with an LGSR reference frame.

2.2.2. Consequences of the differing observational parameters of the LDS and HIPASS

Because the LDS and the HIPASS data do not measure the sky with the same limiting sensitivities, angular resolutions, velocity resolutions, or velocity coverages, the northern population of CHVCs will be differently sampled than the southern one. In particular, the maximum depth of the two samples will be different since the surveys have different limiting fluxes. We describe below how we identify, and compensate for, the differing properties of the two catalogs; we also describe how we sample the simulations using the selection criteria corresponding to the observations. A detailed comparison of objects detected in the two surveys is made in Paper I.

The LDS covered the sky north of declination −30° (the actual declination cut-off varied between −32 and −28°); the angular resolution of the 25–m Dwingeloo telescope was 36′. The effective velocity coverage of the LDS extends over LSR velocities from −450 km s^{-1} to +400 km s^{-1}, resolved into channels 1.03 km s^{-1} wide. The formal rms sensitivity is 0.07 K per 1.0 km s^{-1} channel. Stray radiation has been removed as described by Hartmann et al. (1996). Due to the presence of radio frequency interference, it was important that the reality

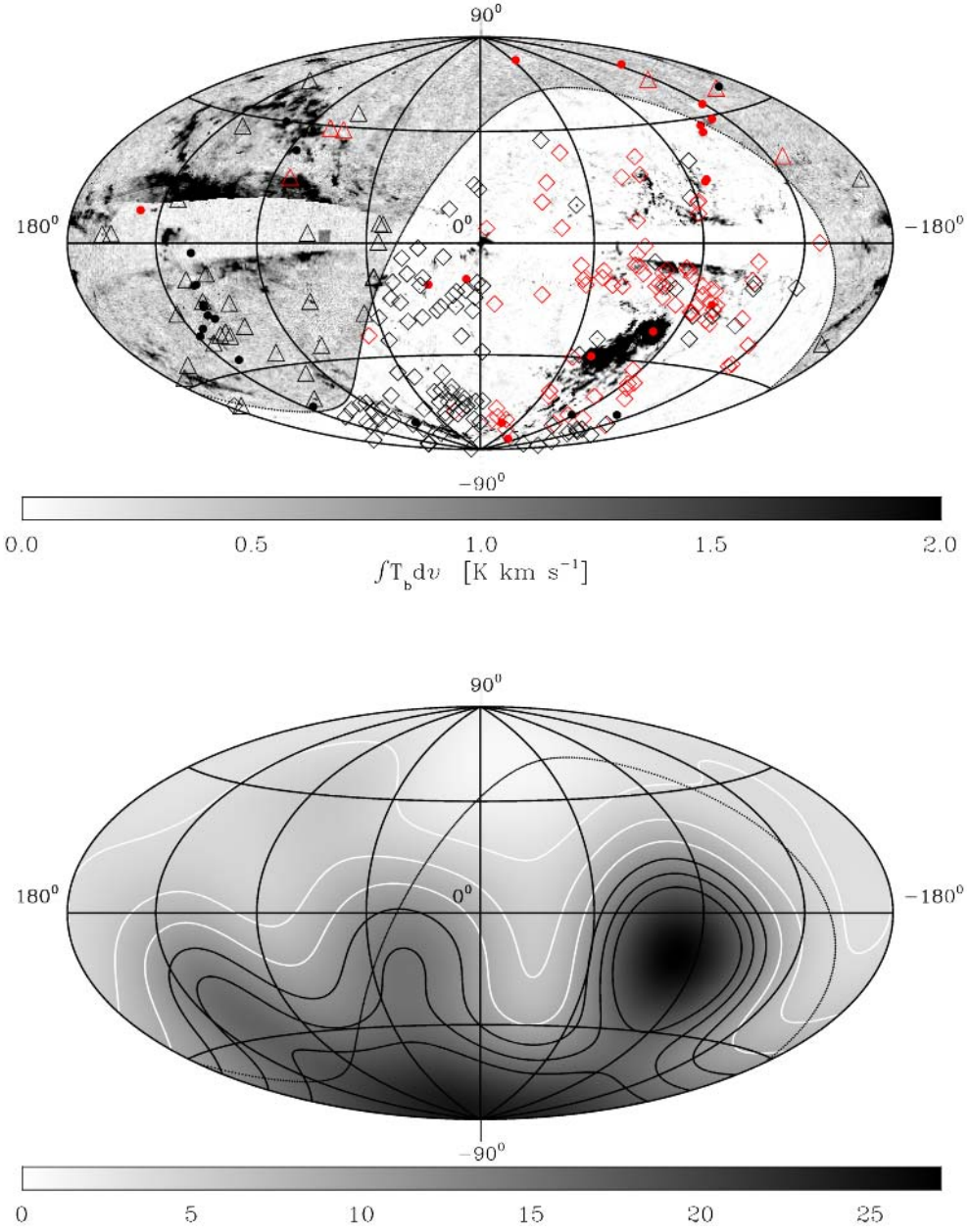

Fig. 5. Spatial deployment of CHVCs over the sky. *Upper panel:* distribution of the cataloged CHVCs, with triangles representing the LDS sample of de Heij et al. (2002) at $\delta > 0°$ and diamonds representing the HIPASS sample of Putman et al. (2002) at southern declinations. Filled circles correspond to the Local Group galaxies listed by Mateo (1998). Red symbols indicate positive LSR velocities and black symbols negative velocities. The background grey–scale shows H I column depths from an integration of observed temperatures over velocities ranging from $V_{\rm LSR} = -450$ km s^{-1} to +400 km s^{-1}, but excluding all gas with $V_{\rm DEV} < 70$ km s^{-1}. *Lower panel:* smoothed relative density field of the CHVCs, accounting for the different observational parameters of the LDS and HIPASS catalogs. The cataloged CHVCs are each represented by a Gaussian with a true–angle dispersion of 20°; the total flux of the Gaussian is set to unity for the LDS objects and to the likelihood of observing such an object in an LDS–like survey for the HIPASS sources. The grey-scale is calibrated in object number per steradian. Contours are drawn at relative densities of −60%, −30%, 0% (in white) and 30%, 60%, 90% (in black). A significant over–density of CHVCs in the southern hemisphere remains after accounting for the different observational parameters. (This figure is available in color in electronic form.)

of all CHVC candidates that were identified in the LDS be independently confirmed. Although interference in the LDS often had the shape of extremely narrow–band signals that are easily recognized as artificial, some types of interference were indistinguishable from naturally occurring features. The reality of the CHVC candidates was either confirmed by the identification of the candidates with objects in independent published material, or by new observations made with the Westerbork Synthesis Radio Telescope, operating as a collection of 14 single dishes.

The HIPASS program covered the sky south of declination +2°. The survey has been reduced in such a way that emission which extends over more than 2° was filtered out. To recover a larger fraction of the extended emission, the part of the

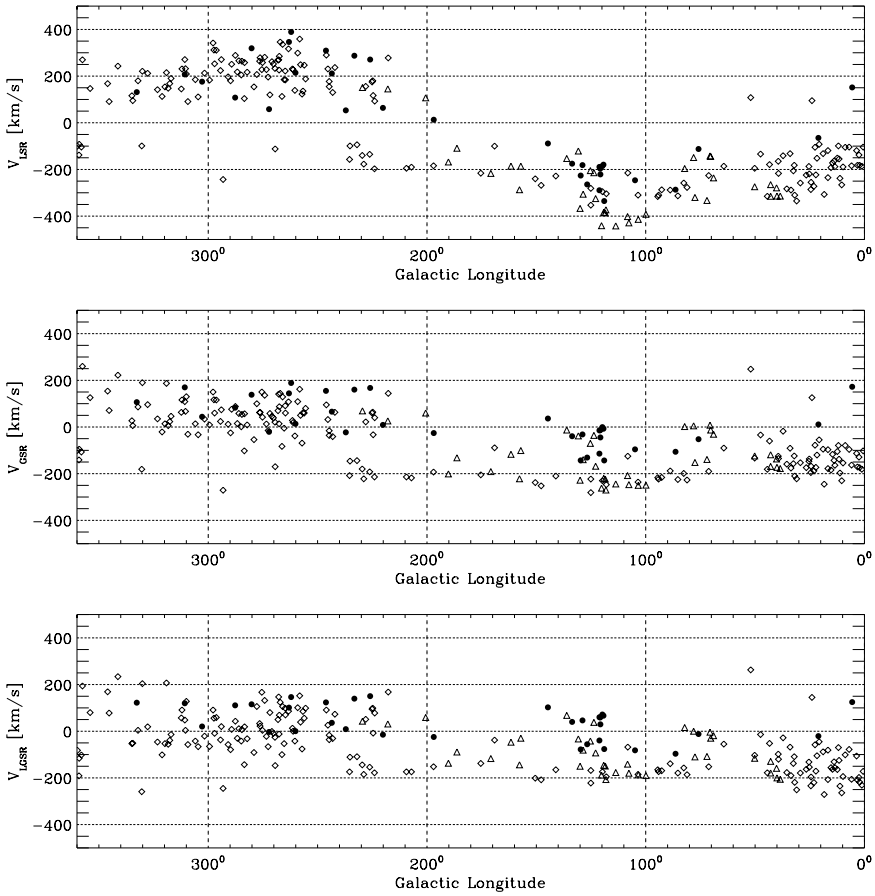

Fig. 6. Kinematic deployment of CHVCs identified in the LDS (triangles) and in the HIPASS (diamonds) data, plotted against Galactic longitude for three different kinematic reference frames, namely the LSR (upper), the GSR (middle), and the LGSR (lower panel). The filled circles show the kinematic deployment with longitude of the Local Group galaxies listed by Mateo (1998). The mean velocities and the dispersions in velocity of the CHVCs and Local Group galaxies are listed in Table 2 for the three reference frames.

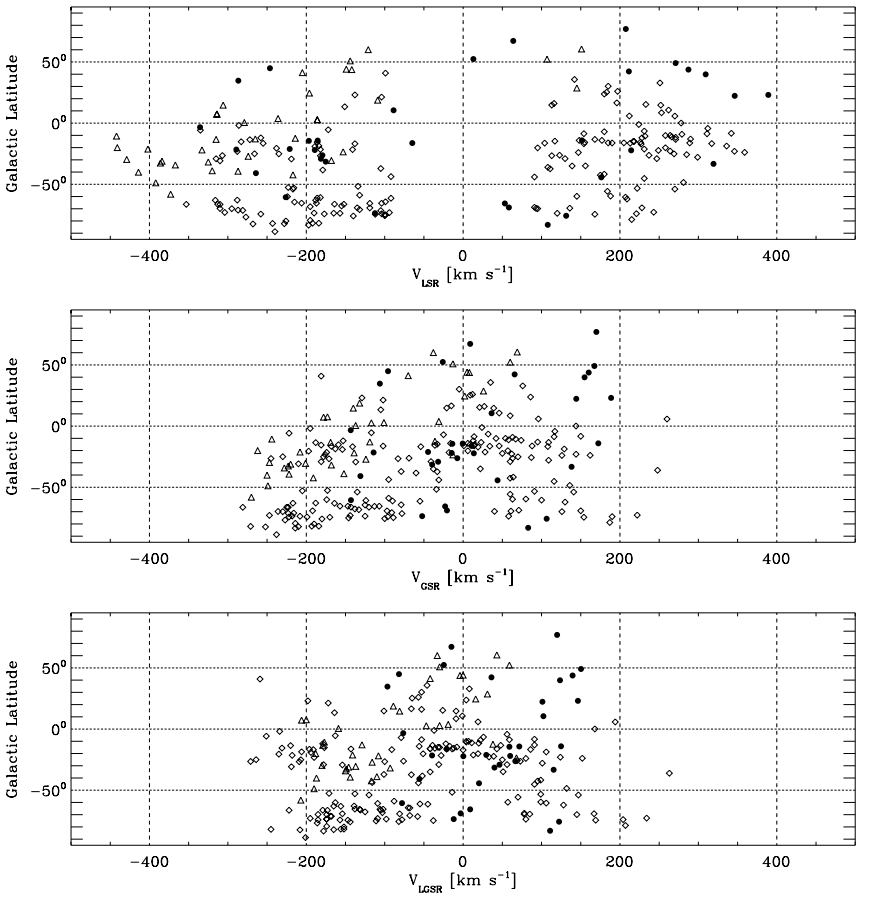

Fig. 7. Kinematic deployment of CHVCs identified in the LDS (triangles) and in the HIPASS (diamonds) data, plotted against Galactic latitude in the three different kinematic reference frames, as in Fig. 6. The filled circles show the kinematic deployment with latitude of the Local Group galaxies listed by Mateo (1998). The mean velocities and the dispersions in velocity of the CHVCs and Local Group galaxies are listed in Table 2 for the three reference frames.

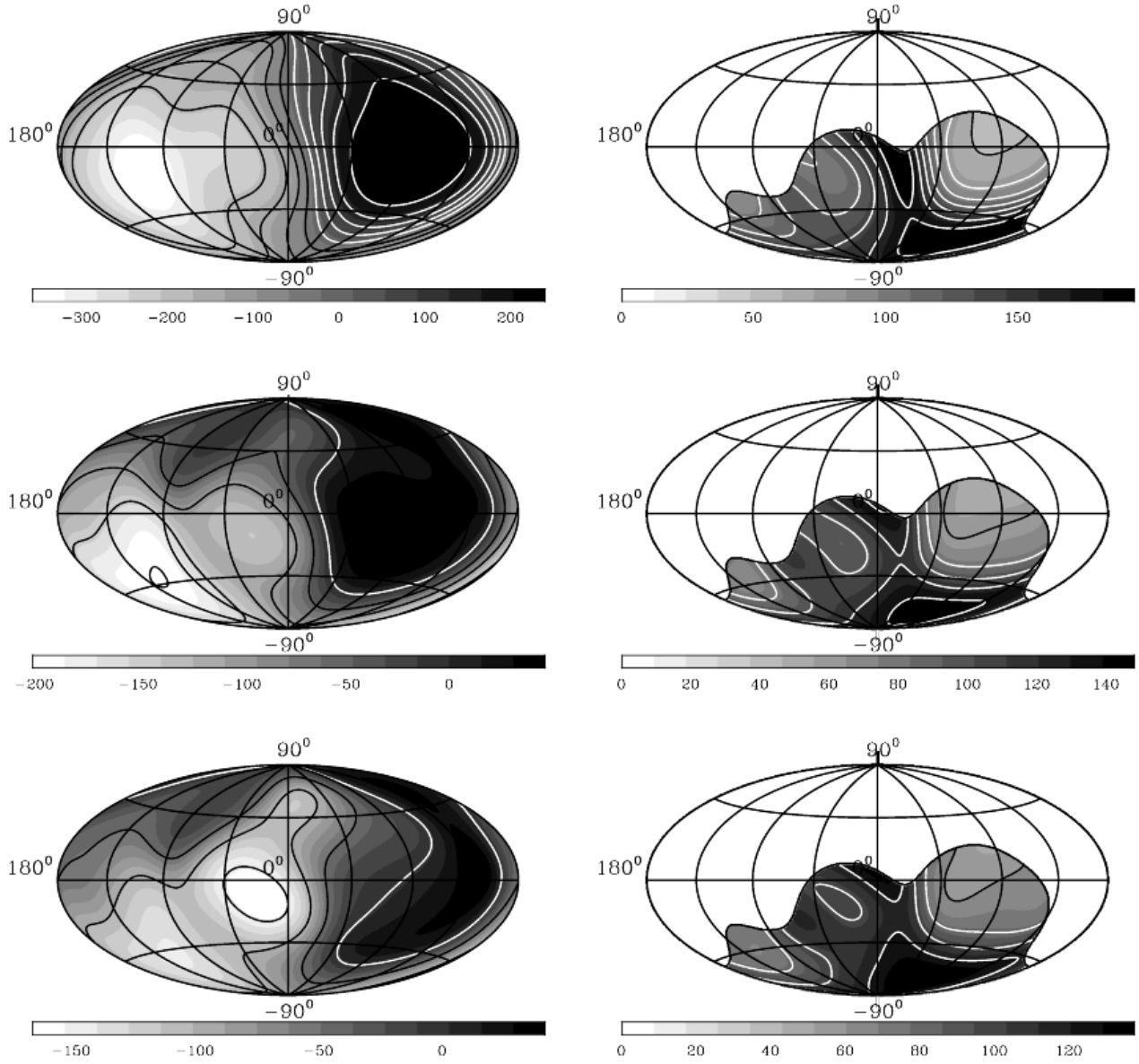

Fig. 8. Smoothed distributions of velocity and velocity dispersion of the CHVC ensemble. The panels on the left show the average velocity in the LSR (upper), GSR (middle), and LGSR (lower) reference frames, respectively. The panels on the right show the velocity dispersions, similarly arranged. Individual CHVCs in the ensemble were convolved with a Gaussian of true–angle dispersion of 20°. White contours for the velocity and dispersion fields are at drawn at values of 0, 50, ... km s^{-1}; black ones are drawn at −50, −100, ... km s^{-1}. These smoothed representations of the observed situation can be compared with similarly sampled and smoothed representations of simulations, as described in the text.

survey which covers LSR velocities ranging from −700 km s^{-1} to +500 km s^{-1} was re–reduced using the MINMED5 method described by Putman (2000), before production of the Putman et al. (2002) catalog. The HIPASS data were gridded with lattice points separated by 4′ with an angular resolution of 15.′5. The HIPASS velocity resolution after Hanning smoothing is 26.4 km s^{-1}, thus substantially coarser than the 1.03 km s^{-1} of the LDS. The HIPASS sensitivity for such a velocity resolution is 10 mK for unresolved sources. Because the observing procedure involved measuring each line of sight five times in order to reach the full sensitivity, all HIPASS sources have effectively been confirmed after median gridding.

Figure 3 shows that the LDS and the HIPASS reflect differing measures of the CHVC properties, because of their differing observational properties. The panel in the upper left of this figure contrasts the observed velocity widths of the LDS and HIPASS samples. The velocity *FWHM* measured in the LDS ranges from about 20 km s^{-1} to some 40 km s^{-1}, with a median of about 25 km s^{-1}. Only for a few sources were values as low as 5 km s^{-1} measured. The relatively high median *FWHM* likely indicates that most of the observed H I in the CHVCs is in the form of warm neutral medium. High–resolution observations of a sample of ten CHVCs made with the 3.′5 resolution afforded by the Arecibo telescope

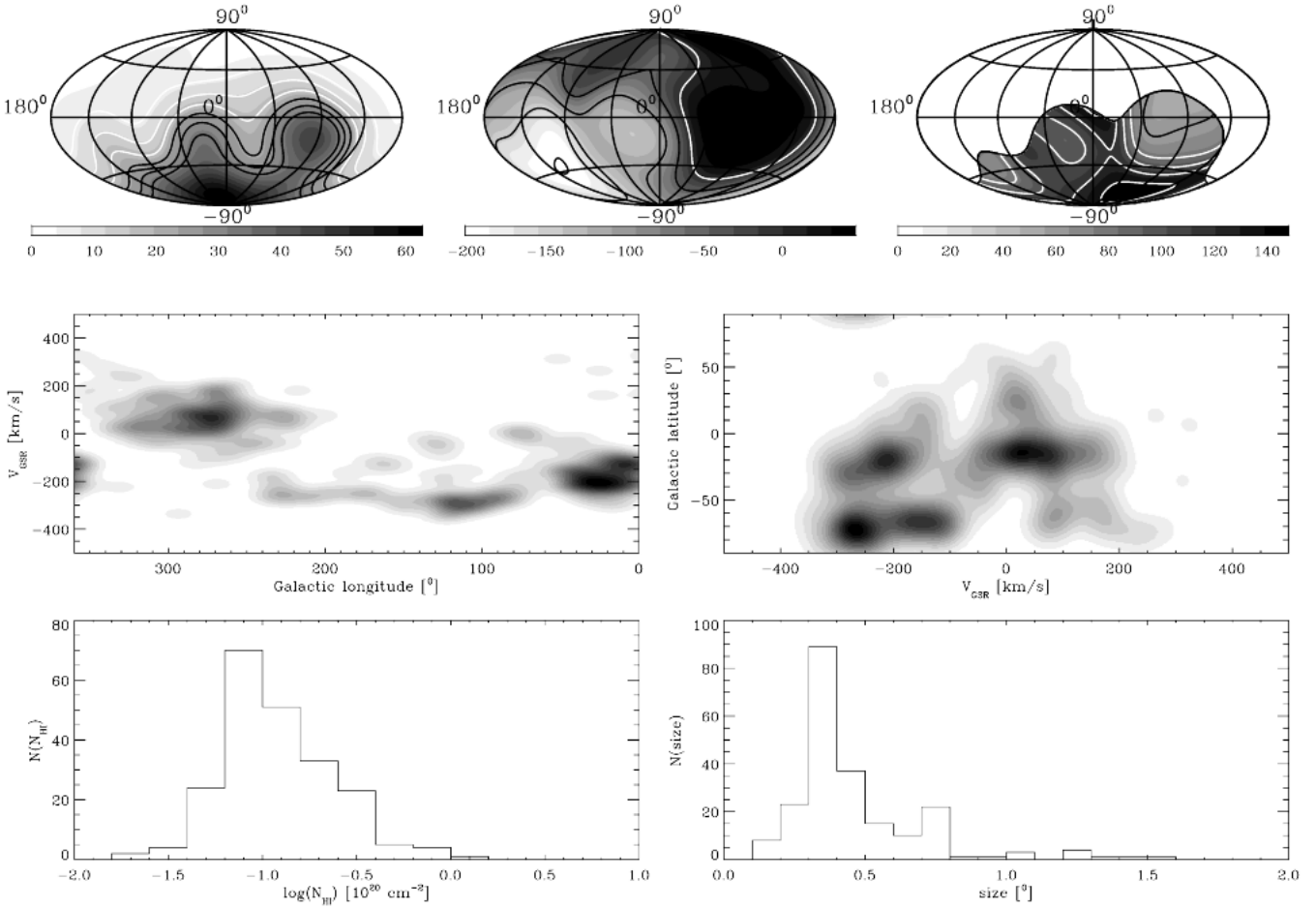

Fig. 9. Summary of the observed spatial, kinematic, angular size, and flux properties of the CHVC ensemble. The three panels arranged across the top of the figure show sky projections, as follows: *left:* smoothed density field of the CHVC population. A Gaussian with a dispersion of 20° (true angle) was drawn at the location of each CHVC; the volume of the Gaussian is unity for both LDS and HIPASS sources – thus in this case the observations are shown directly, i.e. HIPASS sources are *not* weighted by the likelihood with which they would be observed in a LDS–like survey. *Middle:* smoothed velocity field of the population in the Galactic Standard of Rest frame. *Right:* smoothed velocity dispersion field. The grey–scale bar for the left–hand panel is labeled in units of CHVC per steradian; the other two bars are labeled in units of km s^{-1}. Contours are drawn at relative densities of −60%, −30%, 0% (in white) and 30%, 60%, 90% (in black). White contours for the velocity and dispersion fields are at drawn at values of 0, 50, ... km s^{-1}; black ones are drawn at −50, −100, ... km s^{-1}. The two panels in the middle row of the figure show the kinematic distribution of the observed CHVC ensemble, representing $V_{\rm GSR}$ plotted against l and b, as indicated. Delta functions at the observed coordinates were convolved with a Gaussian with an angular dispersion of 20° and velocity dispersion of 20 km s^{-1}. The two lower panels show, respectively, the observed peak H I column density distribution of the CHVC population and the observed angular size distribution.

(Burton et al. 2001) showed warm halos to be a common property of these objects. On the other hand, the median HIPASS velocity width is about 35 km s^{-1} *FWHM*. We can demonstrate that the two observed *FWHM* distributions are consistent with the same object population by convolving the LDS distribution with the HIPASS velocity resolution. The resulting distribution agrees well with that measured in the HIPASS.

The panel in the upper right of Fig. 3 shows histograms of the angular sizes of the cataloged CHVCs, determined from velocity integrated images of each cloud. A contour was drawn at the intensity of half the peak column density of the cloud. After fitting an ellipse to this contour, the size of the cloud was measured as the average of the minor and major axes. It is clear from these distributions that many of the CHVCs are resolved by HIPASS, but that this is rarely the case for the LDS. Some CHVCs in the LDS catalog were only detected in a single spectrum – giving the peak in the histogram at 0.°4, which is an artifact of the sub–Nyquist LDS sky sampling. After convolving the HIPASS distribution with the LDS beam a more similar distribution of sizes is found, although there remains a small excess of relatively large objects in the north.

The panel on the lower left of Fig. 3 shows the flux distribution for the CHVCs detected by HIPASS and the LDS, respectively. An excess of faint sources is present in the HIPASS sample, even after compensation for the lower LDS sensitivity (as outlined below). Conversely, the LDS may have a small excess of bright objects. If semi-isolated objects are considered (i.e. the :HVC and ?HVC categories discussed by Putman et al.

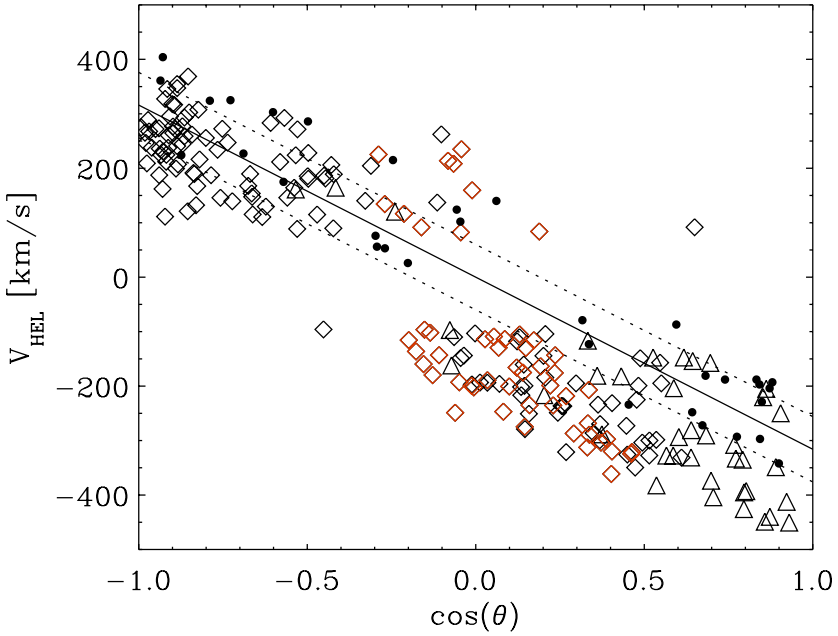

Fig. 10. Variation of heliocentric velocity versus the cosine of the angular distance between the solar apex and the direction of the object; CHVCs from the de Heij et al. (2002) LDS compilation at $\delta > 0°$ are plotted as triangles; those from the Putman et al. (2002) HIPASS compilation, as diamonds. The CHVCs with $b < -65°$ are plotted in red. Local Group galaxies, from the review of Mateo (1998), are indicated by filled circles. The solid line represents the solar motion of $V_\odot = 316$ km s^{-1} towards $l = 93°$, $b = -4°$ as determined by Karachentsev & Makarov (1996). Dashed lines give the $1\sigma(V)$ envelope (± 60 km s^{-1}, following Sandage 1986) encompassing most galaxies firmly established as members of the Local Group. (This figure is available in color in electronic form.)

2002 and de Heij et al. 2002) as in the panel on the lower right of Fig. 3, these differences remain, with the adjusted HIPASS sample showing an excess of faint sources in the south and the LDS sample showing a small excess of brighter sources in the north.

2.2.3. Completeness and uniformity of the CHVC samples

The finite sensitivity of the LDS and HIPASS observations results in sample incompleteness at low flux levels in both surveys. The different sensitivities of the two surveys will bias the derived sky–distribution, average velocity, and velocity dispersion towards the more sensitively observed hemisphere, namely the southern one. To compensate for this bias, the objects found in the southern hemisphere were weighted with the likelihood that they would be detected by a survey with the LDS properties. For this likelihood we use the relation plotted in Fig. 4, following de Heij et al. (2002), who assess the degree of completeness of the LDS catalog as a function of limiting peak brightness from a comparison of the detection rates of cataloged external galaxies over the range $-30° < \delta < 90°$, and from a comparison with the HIPASS catalog of Putman et al. (2002) for the range $-30° < \delta < 0°$. To incorporate plausible uncertainties in this relation, the calculations have also been done for a fictional survey 25% more sensitive, and for one 25% less sensitive, than the LDS, as indicated by the dashed lines in the figure.

Table 1 lists the number of sources with a minimum peak brightness temperature for the northern hemisphere, as observed by the LDS, and for the southern one, as observed by HIPASS. Due to the differences in spectral and spatial resolution, the LDS and HIPASS measure different peak temperatures for the same cloud. For all clouds that are observed in both surveys, the median of the temperature ratio as measured in HIPASS and LDS is 1.5 (de Heij et al. 2002). Applying this temperature scaling to the HIPASS data provides very good agreement with the external galaxy completeness curve of Fig. 4 for declinations $-30°$ to $0°$. However, over the entire HIPASS declination range, the compensated HIPASS data show a strong excess in the source detection rate for sources with an LDS peak temperature in the range 0.2 to 0.4 K. According to Fig. 4, the LDS completeness for these sources should exceed 80%. Therefore the difference in the numbers of relatively faint CHVCs detected by HIPASS and LDS indicates an asymmetry in the distribution upon the sky, with about a factor of two more occurring in the southern hemisphere than in the north. Reducing the sensitivity of the LDS survey by 25% does not change this conclusion.

The CHVC tabulation is probably not incomplete as a consequence of the velocity–range limits of the observational material. Although the part of the LDS that was searched only extended over the range $-450 < V_{\rm LSR} < +350$ km s^{-1}, de Heij et al. (2002) plausibly did not miss many (if any) clouds because of this limited interval. The high–velocity feature with the most extreme negative velocity yet found is that discovered by Hulsbosch (1978) at $V_{\rm LSR} = -466$ km s^{-1}. (This object is listed in Paper I as ?HVC 110.6 – 07.0 – 466: being incompletely sampled in velocity, it does not meet the stringent isolation criteria for the CHVC category, and so does not enter this analysis further.) The Wakker & van Woerden (1991) tabulation, which relied on survey data covering the range $-900 < V_{\rm LSR} < +750$ km s^{-1}, found no high–velocity cloud at a more negative velocity. The HIPASS search by Putman et al. (2002) sought anomalous–velocity emission over the range $-700 < V_{\rm LSR} < +1000$ km s^{-1}. Of the HIPASS CHVCs cataloged by Putman et al., only 10 have $V_{\rm LSR} < -300$, but the most extreme negative velocity is -353 km s^{-1}, for CHVC 125.1 – 66.4 – 353. Regarding the positive–velocity extent of the ensemble, we note that only 7 objects in the HIPASS catalog have $V_{\rm LSR}$ greater than +300 km s^{-1}, and only one has a velocity greater than 350 km s^{-1}, namely CHVC 258.2 – 23.9 + 359.

Table 1. Number of sources with a minimum peak temperature detected in the northern hemisphere and listed in the LDS catalog of de Heij et al. (2002), and in the southern hemisphere and listed in the HIPASS catalog of Putman et al. (2002). Because of the differing angular and velocity resolutions, the two surveys measure different peak temperatures for the same source. The median ratio of HIPASS to LDS peak temperature of 1.5 determined for the sources in common has been used to resample the HIPASS data in the last column.

minimum $T_{\rm peak}$ [K]	$N_{\rm LDS}$ $>T_{\rm peak}$	$N_{\rm HIPASS}$ $>T_{\rm peak}$	$N_{\rm HIPASS}$ $>1.5\,T_{\rm peak}$
1.0	3	5	3
0.5	9	24	9
0.4	12	37	16
0.3	20	56	29
0.2	30	85	56
0.1	38	160	115

All of the 7 CHVCs with substantial positive velocities are near $(l, b) = (270°, 0°)$, where Galactic rotation contributes to a high positive LSR velocity. Since this extended region has a negative declination, it is sampled with the wider velocity coverage of HIPASS, rather than that of the LDS. In view of these detection statistics, we consider it unlikely that the velocity–range limits of either the LDS or of the HIPASS have caused a significant number of CHVCs to be missed. In other words, the true velocity extent, as well as the non–zero mean in the LSR frame, of the anomalous–velocity ensemble are well represented by the observed extrema of -466 km s^{-1} and $+359$ km s^{-1}.

The strong concentration of faint CHVCs with an extreme variation in their radial velocity in the direction of the south Galactic pole was already noted by Putman et al. (2002). A complete model for the all-sky distribution of objects will need to reproduce the enhancement in numbers as well as local velocity dispersion in this direction. Much of the north–south detection asymmetry for faint CHVCs remains even after excluding all objects with a Galactic latitude less than $-65°$, as we discuss in detail below.

3. All–sky spatial, kinematic, and column density properties of the CHVC ensemble

We show in this section the basic observational data for the all–sky properties of the CHVCs; specifically, the deployment in position and velocity as well as the perceived size and H I column density distributions. These basic properties constitute the observables against which the simulations described in the following sections are tested.

3.1. Distribution of CHVCs on the sky

Figure 5 shows the all–sky distribution of the cataloged CHVCs superimposed on the integrated H I emission observed in the range $-450 < V_{\rm LSR} < +400$ km s^{-1}, but with $V_{\rm DEV} > 70$ km s^{-1}. The LDS catalog and data are used in the north and the HIPASS catalog and data in the south, with a solid line marking the demarcation at $\delta = 0°$ separating the LDS from the HIPASS material. Red symbols indicate positive LSR velocities and black symbols negative velocities[1] The much higher object density observed in the southern hemisphere is quite striking, as is the absence of diffuse emission in the HIPASS MINMED5 data. We comment further below on the extent to which the CHVC density is a consequence of the differing observational parameters, especially that of sensitivity.

To get a better impression of the CHVC clustering and distribution on the sky, an average density field is constructed; this smoothed field is more appropriate for comparison with simulated fields, which, as indicated below, are similarly smoothed. A field of delta functions at the CHVC locations was convolved with a Gaussian with a dispersion of 20°. The total flux of each delta function is set to unity for the LDS sources and to the value of the likelihood that such a particular CHVC would be observed in an LDS–like survey for the HIPASS sources. Changes in the likelihood relation do not change the overall picture of the CHVC concentrations; only the contrasts of the overdensity regions with respect to the average changes.

Figure 5 shows that the projected density of CHVCs displays a number of local enhancements. The three most prominent of these occur in the southern hemisphere, and were previously noted by Putman et al. (2002) as Groups 1 through 3. Group 1 is concentrated at the south Galactic pole and extends from about $b = -60°$ to $-90°$. It is remarkable for possessing a local velocity dispersion in excess of 150 km s^{-1}, about twice that seen in any other part of the sky. This region is bisected by a portion of the Magellanic Stream and is also spatially coextensive with the nearest members of the Sculptor group of galaxies (with $D \sim 1.5$ Mpc). Group 2 is located near $(l, b) \sim (280°, -15°)$, with an extent of about 30°. This concentration is approximately in the direction of the leading arm of the Magellanic Clouds but is also near the Local Group anti-barycenter direction, where the Blitz et al. (1999) model predicts an enhancement of high–velocity clouds. Group 3 is centered near $(l, b) \sim (30°, -15°)$, a region that Wakker & van Woerden (1991) have identified with the GCN (Galactic Center Negative velocity) population. The most diffuse concentration, which we label Group 4, is in the northern sky near $(l, b) \sim (115°, -30°)$, approximately coinciding with the Local Group barycenter. The Blitz et al. (1999) model also predicts an enhancement of high–velocity clouds here, albeit a stronger one than observed. Likewise the mini–halo simulations of Klypin et al. (1999), Moore et al. (1999, 2001), and Putman & Moore (2002) predict a strongly enhanced density of low mass objects around the major galaxies of the Local Group, in particular toward M 31, which lies close to the barycenter direction. We comment further on the expected strength of such an enhancement in the observed distribution below.

3.2. Distribution of CHVCs in velocity

The kinematic properties of the CHVC population provide an important constraint that must be reproduced by a successful

[1] Several of the figures in this paper make color-coded distinctions; although the printed journal and electronic versions will display the color coding, black-and-white printouts will not, of course.

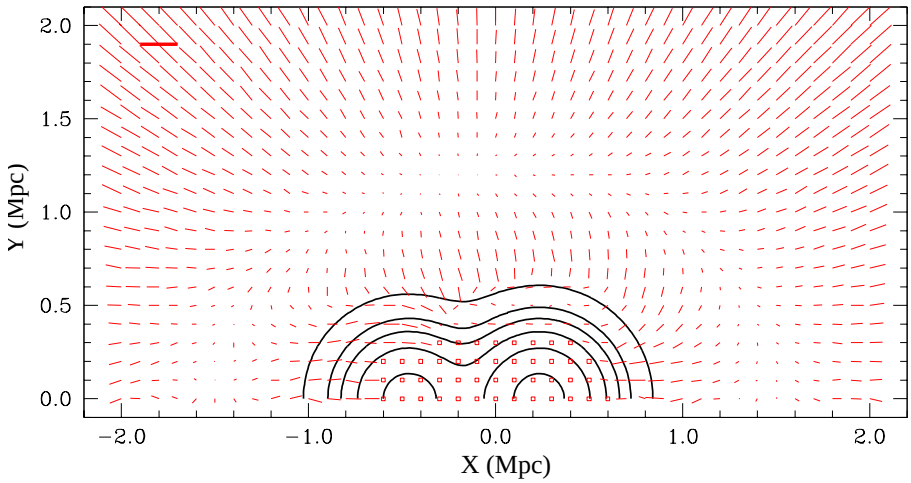

Fig. 11. Average velocity field in the Local Group entering the simulations described in Sect. 4. The velocity at each grid point is given by the average velocity of all the test particles located in a box centered on the grid point and with a width of 10 kpc. Squares are drawn if the velocity dispersion of the ensemble of particles exceeds 100 km s^{-1}. The length of the thick line in the upper left corresponds to a velocity of 200 km s^{-1}. The image corresponds to a simulation with a Local Group mass of 4.3×10^{12} $M_\odot$. The Milky Way and M 31 are located at ($x = -0.47, y = 0.0$ Mpc) and ($x = 0.23, y = 0.0$ Mpc), respectively. The contours show the relative density levels of a combination of two Gaussian distributions with 200 kpc dispersion, centered on the Milky Way and M 31 at 1, 5, 10, 20, 40, and 80% of the peak. (This figure is available in color in electronic form.)

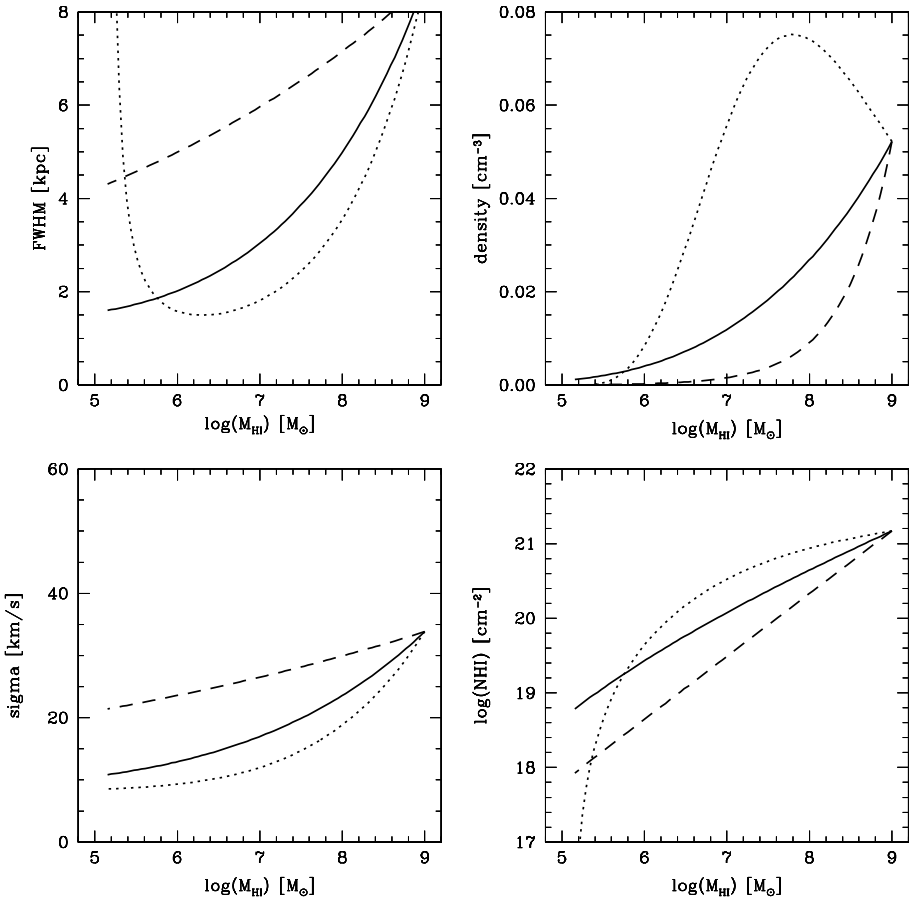

Fig. 12. Properties of the CHVCs entering the simulations described in Sect. 4. Plotted as a function of H I mass, the images show the *FWHM* of the H I distribution, the central H I volume density, the velocity dispersion of the gas, and the peak column density. Details of the relation between the H I masses and cloud properties depend on the dark-matter fraction via the power-law slope of the H I mass distribution of the CHVC population being modeled: the dashed lines in the images correspond to a slope $\beta = -1.2$; the solid lines, to a slope of −1.6; and the dotted lines, to a slope of −2.0.

model of the phenomenon. The kinematic distribution is plotted against Galactic longitude and latitude, for the Local, Galactic, and Local Group kinematic reference frames in Figs. 6 and 7, respectively. The CHVCs are confined within a kinematic envelope narrower in extent than the $V_{\rm LSR}$ spectral coverage of the surveys; we stressed above in Sect. 2.2.3 that this confinement is not a selection effect; it is one of the global kinematic properties of the ensemble which must be accounted for.

Table 2 shows that the ensemble of clouds has a lower velocity dispersion in both the GSR and LGSR systems, compared to that measured in the LSR frame, suggesting that either the Galaxy or the Local Group might be the natural reference system of the CHVCs. By measuring the dispersion in the LSR

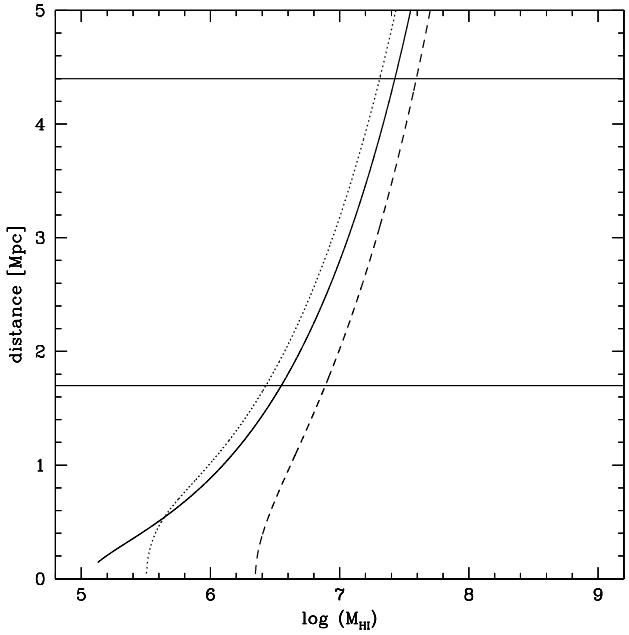

Fig. 13. Distances out to which simulated CHVCs would be detected in the HIPASS survey. The relation between the H I masses and maximum observable distance depends on the dark–matter fraction via the slope of the H I mass distribution of the CHVC population. The three curves refer to clouds with a mass–distribution slope of $-2.0, -1.6$, and -1.2, as dotted, solid, and dashed lines, respectively. The $\beta = -1.2$ clouds are so diffuse that they fall below the HIPASS detection threshold for $\log(M_{\rm HI}) \lesssim 6.4$. The horizontal lines bracket distances to individual Sculptor Group galaxies.

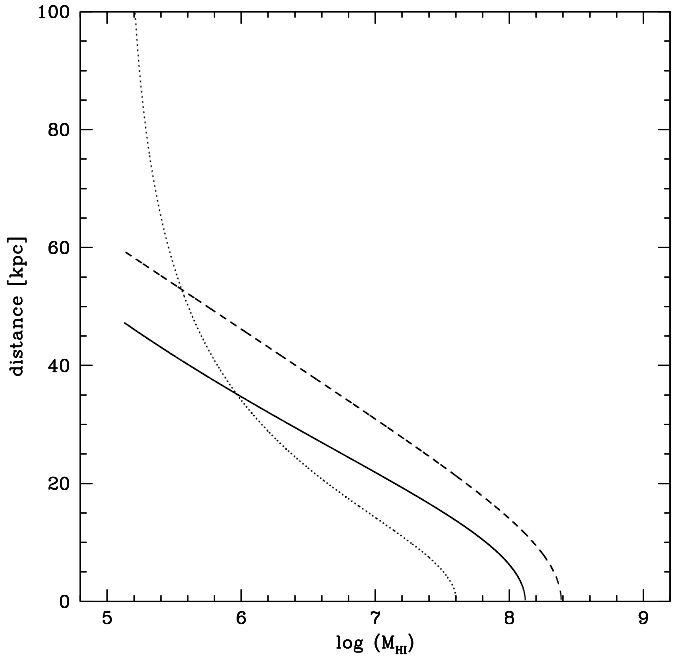

Fig. 14. Distances up to which simulated CHVCs of the indicated total H I masses would be destroyed by ram–pressure stripping in the Galactic halo. As an illustration, the limiting distance is calculated assuming a relative velocity of 200 km s^{-1}. The relation between the H I masses and the stripping distance depends on their dark–matter content via the slope of the H I mass distribution of the CHVC population. The dotted curve corresponds to a slope of $\beta = -2.0$, the solid curve to $\beta = -1.6$, and the dashed one to a slope of -1.2.

frame, one introduces the solar motion around the Galactic center into the velocities, which results in a higher dispersion.

The CHVC groups noted in the previous subsection can also be identified in the (l, V) and (b, V) distributions. Group 1 is best seen in Fig. 7 where it gives rise to the very broad velocity extent in both the GSR and LGSR frames for $b < -60°$. Group 2, on the other hand, is best seen in Fig. 6, centered near $l = 280°$. This group has a positive mean velocity in the GSR frame. Only by going to the LGSR frame does the mean group velocity approach zero. Group 3 is evident in both Figs. 6 and 7. This concentration is seen near $l = 30°$ and has a remarkably high negative velocity of about -200 km s^{-1} in both the GSR and LGSR frames. Group 4 can also be distinguished near $l = 115°$ in Fig. 6. This group also retains a large negative velocity in both the GSR and LGSR frames.

Table 2 gives the all–sky statistical parameters of the CHVC ensemble, calculated by weighting the HIPASS objects with the likelihood that they would be observed in an LDS–like survey. The variation of these parameters with the (flux–dependent) relative weighting of the HIPASS sub–sample is explored by considering both 25% higher and lower relative sensitivity. Although the dispersion is not affected strongly by the weighting given to the HIPASS sub–sample, the mean velocity becomes increasingly negative as the fainter HIPASS sub–sample receives a higher relative weight.

CHVCs near the galactic equator display the horizontal component of their space motion. Figure 7 shows that the radial motions at low $|b|$ are at least as large as those at high latitudes, and furthermore that the CHVC distribution does not avoid the Galactic equator, and that substantial positive–velocity amplitudes, as well as negative–velocity ones, are observed. Large horizontal motions as well as high positive velocities are difficult to account for in terms of a galactic fountain model (e.g. Shapiro & Field 1976; Bregman 1980). Similarly, CHVCs located near the galactic poles offer unambiguous information on the vertical, z, component of their space motion. The vertical motions are substantial, with positive velocities approximately equal in number and amplitude to negative velocities; the vertical motions are of approximately the same amplitude as the horizontal ones. This situation also is incompatible with the precepts of the fountain model, which predicts negative V_z velocities for material returning in a fountain flow. Furthermore, the values of V_z are predicted to not exceed the velocity of free fall, of some 200 km s^{-1}. In fact, $V_{\rm LSR}$ amplitudes substantially larger than the free–fall value are observed.

Several aspects of the spatial and kinematic topology of the class are difficult to account for if the CHVCs are viewed as a Milky Way population, in particular if they are viewed as consequences of a galactic fountain; these same aspects would seem to discourage a revival of several of the mechanisms suggested earlier for a Milky Way population of high–velocity

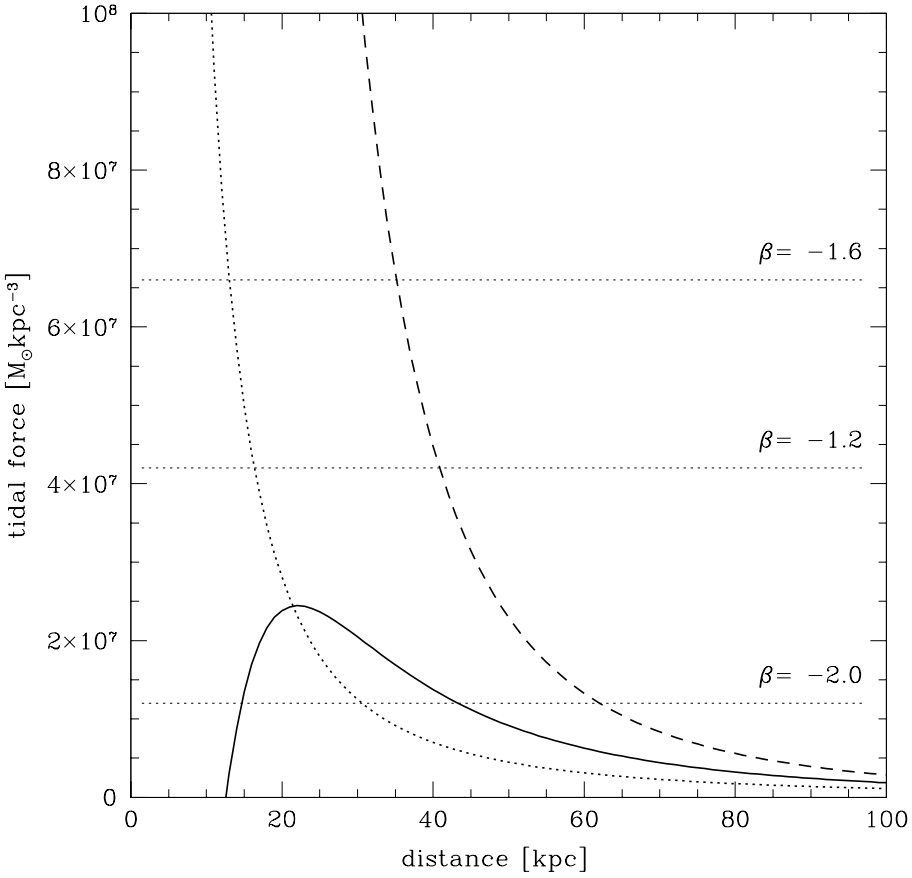

Fig. 15. Tidal force for different potentials as a function of Galactocentric distance. The dashed line corresponds to a point source with the mass of the Milky Way, the dotted line corresponds to a potential consistent with a rotation curve flat at the level of 220 km s^{-1}, while the solid line corresponds to the isochrone potential which is used in the simulations to describe the Milky Way. The dashed horizontal lines correspond to the indicated H I mass slopes for a cloud mass of $M_{\rm HI} = 10^5\ M_\odot$. Only for this low cloud mass and the low dark–matter fraction implied by $\beta = -2$ are clouds unstable to tidal disruption.

clouds (reviewed, for example, by Oort 1966), including ejection from the Galactic nucleus, association with a Galactic spiral arm at high latitude, and ejection following a nearby supernova explosion. We note that the spatial deployment plotted Fig. 5 shows no preference for the Galactic equator, nor for the longitudes of the inner Galaxy expected to harbor most of the disruptive energetic events. CHVCs do not contaminate the H I terminal–velocity locus in ways which would be expected if they pervaded the Galactic disk; this observation constrains the clouds either to be an uncommon component of the Milky Way disk, confined to the immediate vicinity of the Sun, or else to be typically at large distances beyond the Milky Way disk. We note also that the lines of sight in the directions of each of the low $|b|$ CHVCs traverse some tens of kpc of the disk before exiting the Milky Way: unless one is prepared to accept these CHVCs as boring through the conventional disk at hypersonic speeds (for which there is no evidence), and atypical in view of the cleanliness of the terminal–velocity locus, then their distance is constrained to be large. We note further that some of the CHVC objects are moving with velocities in excess of a plausible value of the Milky Way escape velocity (cf. Oort 1926).

Figure 8 shows the average velocity field and velocity dispersion field, which is constructed in the same way as the average density field. A field of delta functions was convolved with a Gaussian with a dispersion of 20°. The flux of each delta function was set equal to the measured CHVC velocity and multiplied by the likelihood that the CHVC would be observed in an LDS–like survey. The convolved image was then normalized by the density field. For the velocity dispersion field, a gridded distribution of squared velocity was similarly generated and the velocity dispersion was calculated from the square root of the mean squared velocity less the mean velocity squared, $\sigma = \sqrt{(< V^2 > - < V >^2)}$. The velocity dispersion field was blanked where the normalized density was below the mean, since insufficient objects otherwise contribute to the measurement of local dispersion.

Kinematic patterns in the LSR velocity field are dominated by the contribution of Galactic rotation. After removing the contribution of Galactic rotation by changing to the GSR reference frame, the following characteristics of the kinematics of the groups are evident. Relative minima of $V_{\rm GSR} = -100$ to -175 km s^{-1} are seen in the directions of Groups 3 and 4, and a relative maximum of $V_{\rm GSR} = +45$ km s^{-1} is seen in the vicinity of Group 2. Transforming to the LGSR frame generally lowers the magnitude of these kinematic properties (except in the case of Group 3 which becomes more negative in velocity) although they are all still present. The relative velocities of Groups 2, 3, and 4 fit into a coherent global pattern shared by much of the CHVC population, consisting of a strong gradient in the GSR and LGSR velocity that varies from strongly negative below the Galactic plane in the first and second quadrants to near zero in the third and fourth quadrants near the plane.

The distribution of velocity dispersion is not as strongly effected by the choice of reference frame since it is a locally defined quantity. The exception to this rule is near $l = 0°$, where there are large gradients in the velocity field, leading to larger

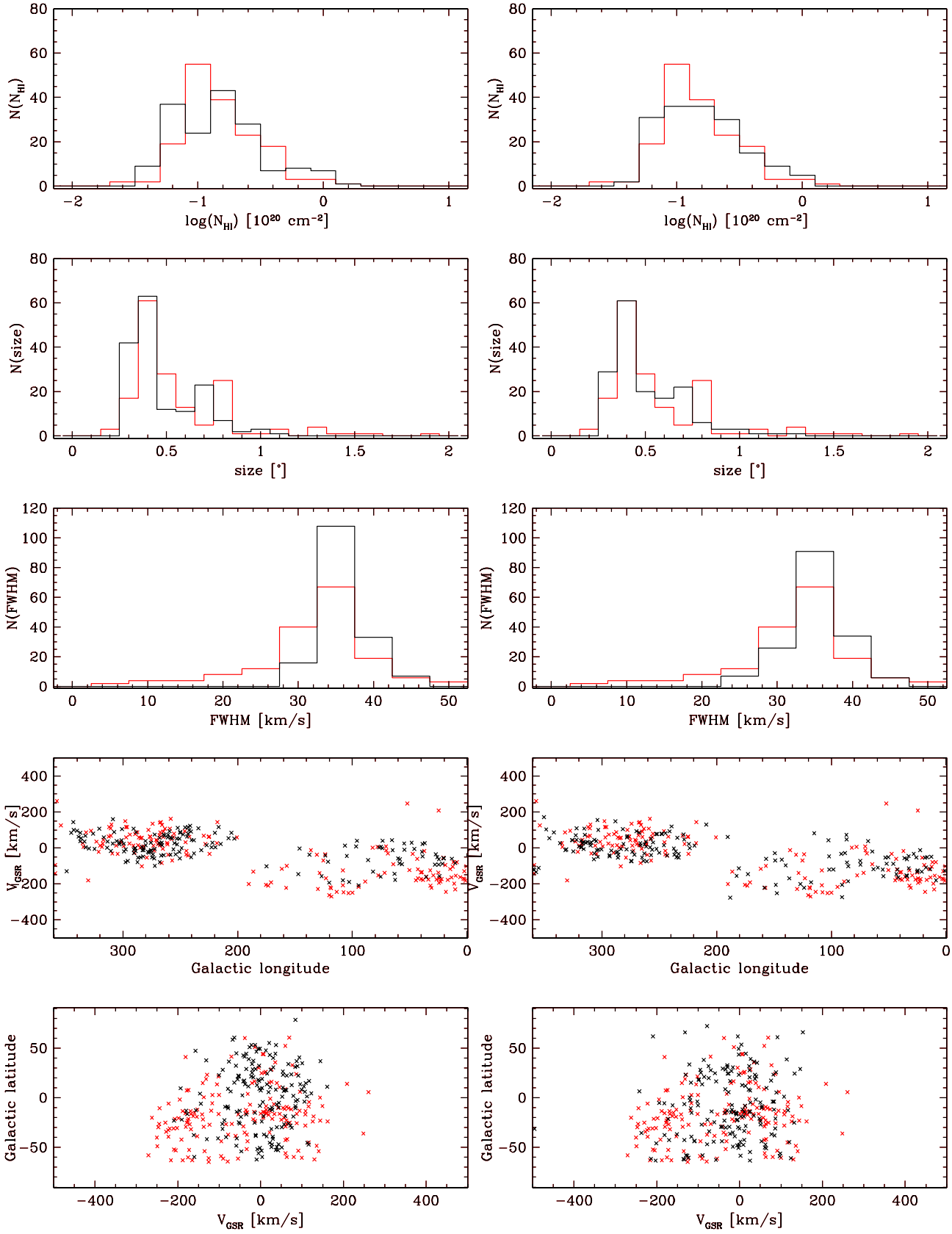

Fig. 16. Demonstration of the effects of shot–noise on fit quality, showing the best– and worst–fitting instances from a sequence of 35 simulations with one of the lowest average χ^2 values. The parameter values are $M_1 = 10^7\ M_\odot$, $\beta = -1.7$, and $\sigma_d = 200$ kpc, corresponding to model #9 from Table 4. The best–fitting instance is plotted on the right and the worst–fitting on the left. Black lines and symbols are used for the simulations and red for the observations. Values of χ^2 from top to bottom for the best-fitting case are 1.5, 2.2, 3.2, 0.19, and 0.21, respectively; while for the worst-fitting case these are 3.5, 3.3, 5.5, 0.29, and 0.36. (This figure is available in color in electronic form.)

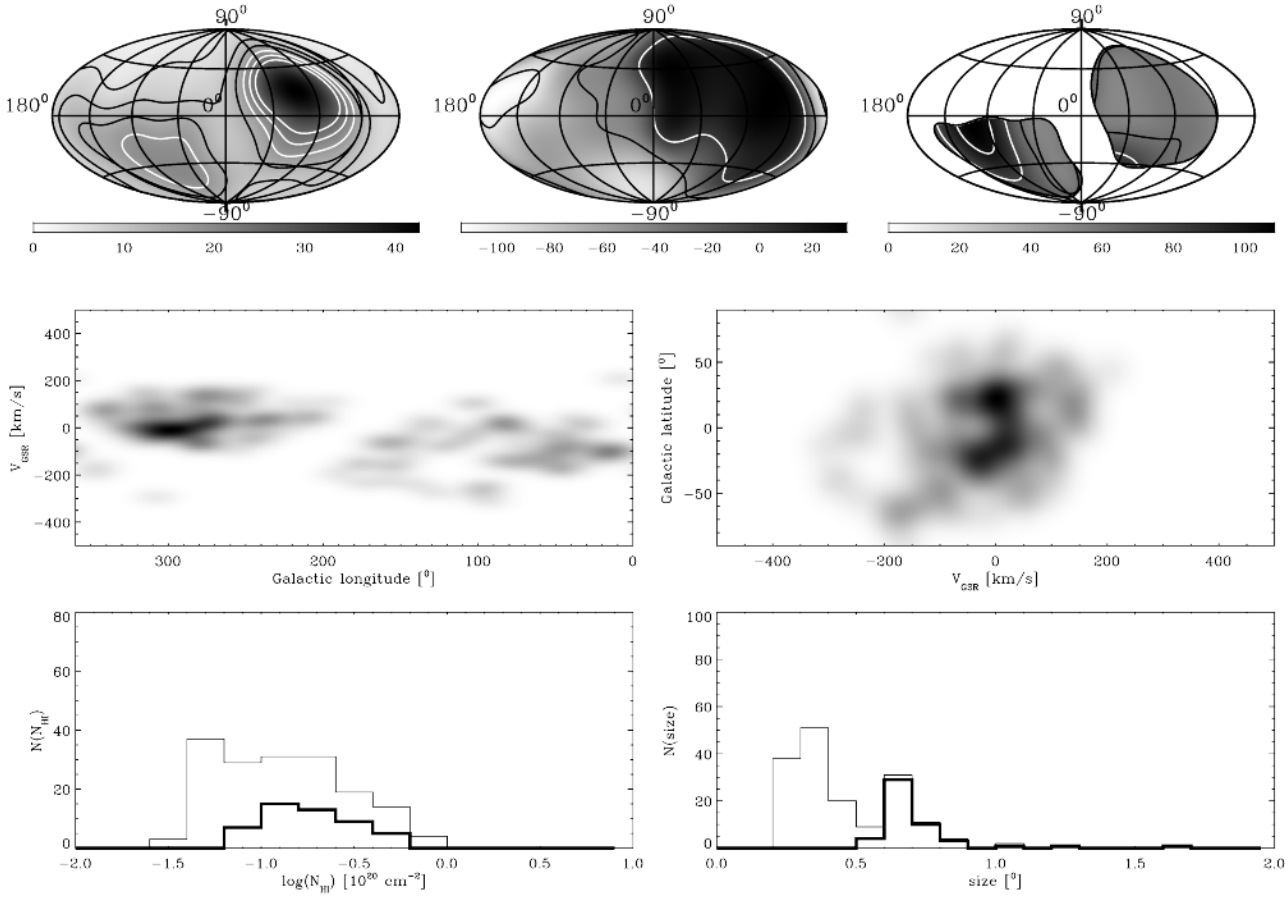

Fig. 17. Overview of the spatial and kinematic properties of one of the best fitting Local Group models from the simulations of Sect. 4. The simulation, model #9 in Table 4, has the following parameters: $M_1 = 10^7\ M_\odot, \beta = -1.7$, and $\sigma_d = 200$ kpc. The quality of the fit to the various observables is given by $\chi^2(\text{size}) = 2.3, \chi^2(N_{\rm HI}) = 2.9, \chi^2\ (FWHM) = 4.1, \chi^2(l,b) = 0.28, \chi^2(l, V_{\rm GSR}) = 0.24$, and $\chi^2(V_{\rm GSR}, b) = 0.29$. The panels provide the same information as the panels in Fig. 9 for the observed data. The simulation was sampled with the observational parameters of the LDS and HIPASS surveys, depending on the declination of the test cloud, as discussed in the text. The thick–line histograms indicate the LDS (northern hemisphere) contributions to the total detections.

apparent dispersions when sampled with our smoothing kernel. Group 1 is remarkable for its extremely high velocity dispersion, exceeding that of Groups 2–4 by a factor of two or more. It is plausible that the Group 1 concentration represents a somewhat different phenomenon than the remainder of the CHVC sample, as we discuss further below.

3.3. Summary of the basic observables of the CHVC ensemble

In the preceding sub–sections we have attempted to correct for the differing detection levels in the northern and southern hemisphere data to produce a spatially unbiased estimate of the CHVC distributions in position and velocity. However, when making comparisons with model calculations it is possible to explicitly take account of the differing resolutions and sensitivity of the data in the north and south, obviating the need to re–weight portions of our sample in advance. The basic observables from our all–sky sample of CHVCs, without re–weighting, are shown in Fig. 9 relative to the GSR frame. The top row of panels represents the density, velocity, and velocity-dispersion fields, just as in Figs. 5 and 8, except that the HIPASS sub–sample has not been re-weighted relative to the LDS. Smoothed versions of the (l, V) and (V, b) plots shown in Figs. 6 and 7 are shown in the middle panels of Fig. 9 to facilitate comparison with the model distributions discussed below. The distribution of delta functions was convolved with a Gaussian with a dispersion of 20° in angle and 20 km s^{-1} in velocity. Composite histograms of the peak column density and angular size distributions for the whole sky are shown in the lower panels of Fig. 9. Since the LDS and HIPASS survey resolutions are different (as discussed above in Sect. 2.2.2) these observables have a different physical implication in the two hemispheres, but again, these differences can be accounted for explicitly in the comparison with model distributions.

4. A Local Group population model for the CHVC ensemble

Determining Local Group membership for nearby galaxies is not a trivial undertaking. The well–established members of the Local Group have been used to define a mass–weighted Local Group Standard of Rest, corresponding to a solar motion of $V_\odot = 316$ km s^{-1} towards $l = 93°$, $b = -4°$

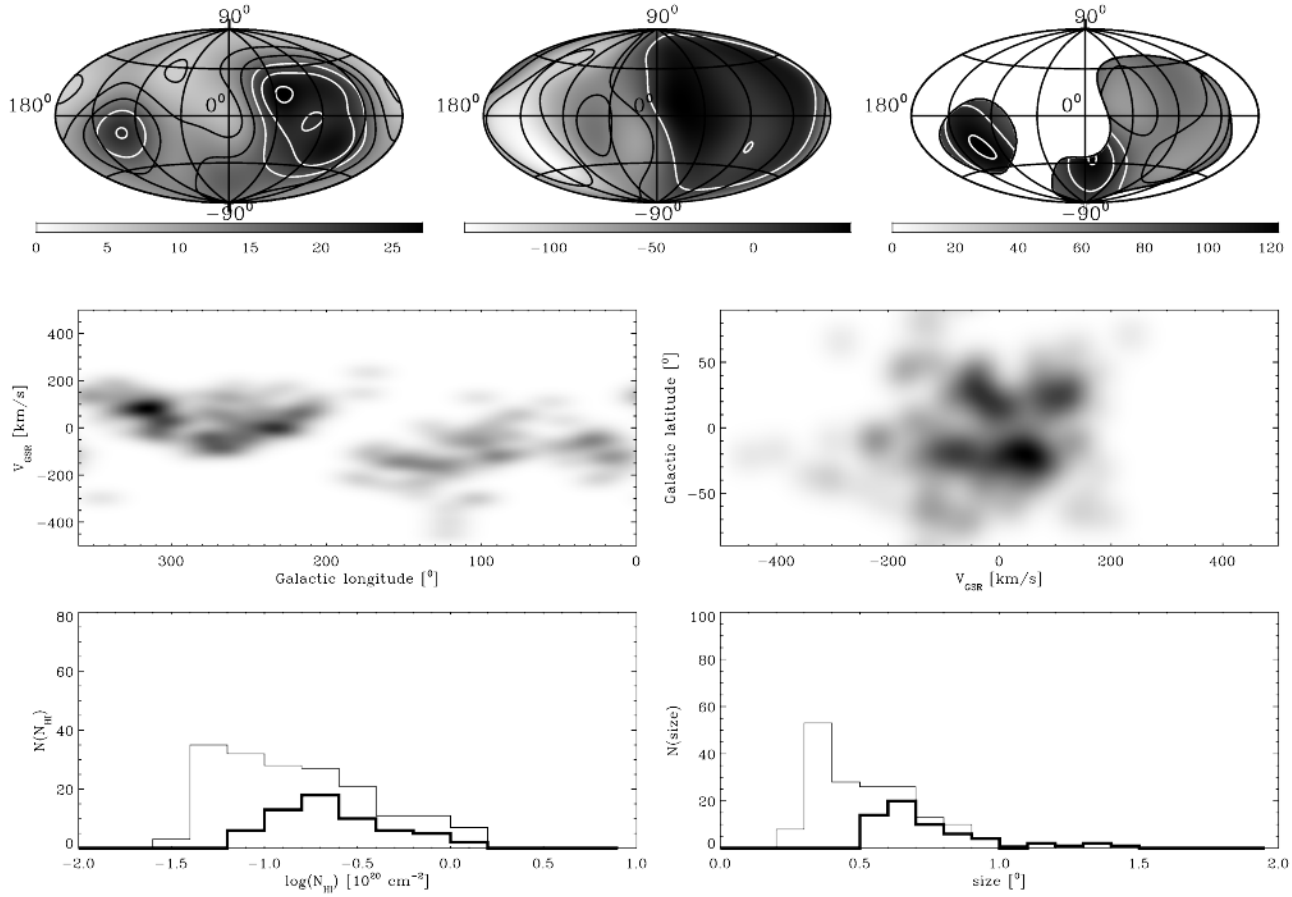

Fig. 18. Overview of the spatial and kinematic properties of one of the best fitting Local Group models from the simulations of Sect. 4. The simulation, model #3 in Table 4, has the following parameters: $M_1 = 10^{7.5}\ M_\odot$, $\beta = -1.7$, and $\sigma_d = 150$ kpc. The quality of the fit is characterized by $\chi^2(\text{size}) = 2.6$, $\chi^2(\text{N}_{\text{HI}}) = 2.7$, $\chi^2\ (FWHM) = 3.9$, $\chi^2(l,b) = 0.25$, $\chi^2(l, V_{\text{GSR}}) = 0.21$, and $\chi^2(V_{\text{GSR}}, b) = 0.25$. The panels provide the same information as the panels in Fig. 9 for the observed data. The thick–line histograms indicate the LDS (northern hemisphere) contributions to the total detections.

(Karachentsev & Makarov 1996). The 1σ velocity dispersion of Local Group galaxies with respect to this reference frame is about 60 km s^{-1} (Sandage 1986). A plot of heliocentric velocity versus the cosine of the angular distance between the solar apex and the galaxy in question, as shown in Fig. 10, has often been used to assess the likelihood of Local Group membership (e.g. van den Bergh 1994) when direct distance estimates have not been available. Local Group galaxies tend to lie within about one sigma of the line defined by the solar motion in the LGSR reference frame. Braun & Burton (1999) pointed out how the original LDS CHVC sample followed this relationship, although offset with a significant infall velocity. The all–sky CHVC sample has been plotted in this way in Fig. 10. Both the sample size and sky coverage are significantly enhanced relative to what was available to Braun & Burton. A systematic trend now becomes apparent in the CHVC kinematics. While the CHVCs at negative $\cos(\theta)$ (predominantly in the southern hemisphere) tend to lie within the envelope defined by the LGSR solar apex and the Local Group velocity dispersion, the CHVCs at positive $\cos(\theta)$ have a large negative offset from this envelope. Obscuration by Galactic H I may well be important in shaping this trend. Only by analyzing realistic model populations and subjecting them to all of the selection and sampling effects of the existing surveys can meaningful conclusions be drawn.

Recently several simulations have been performed to test the hypothesis that the CHVCs are the remaining building blocks of the Local Group. Putman & Moore (2002) compared the results of the full *N*–body simulation described by Moore et al. (2001) with various spatial and kinematic properties of the CHVC distribution, as well as with properties of the more general HVC phenomenon, without regard to object size and degree of isolation. Putman & Moore were led to reject the Local Group deployment of CHVCs, for reasons which we debate below. Blitz et al. (1999) performed a restricted three body analysis of the motion of clouds in the Local Group. In their attempt to model the HVC distributions, Blitz et al. modeled the dynamics of dark matter halos in the Local Group and found support for the Local Group hypothesis when compared qualitatively with the deployment of a sample of anomalous–velocity H I containing most HVCs, but excluding the large complexes (including the Magellanic Stream) for which plausible or measured distance constraints are available. Assuming that 98% of the Local Group mass is confined to the Milky

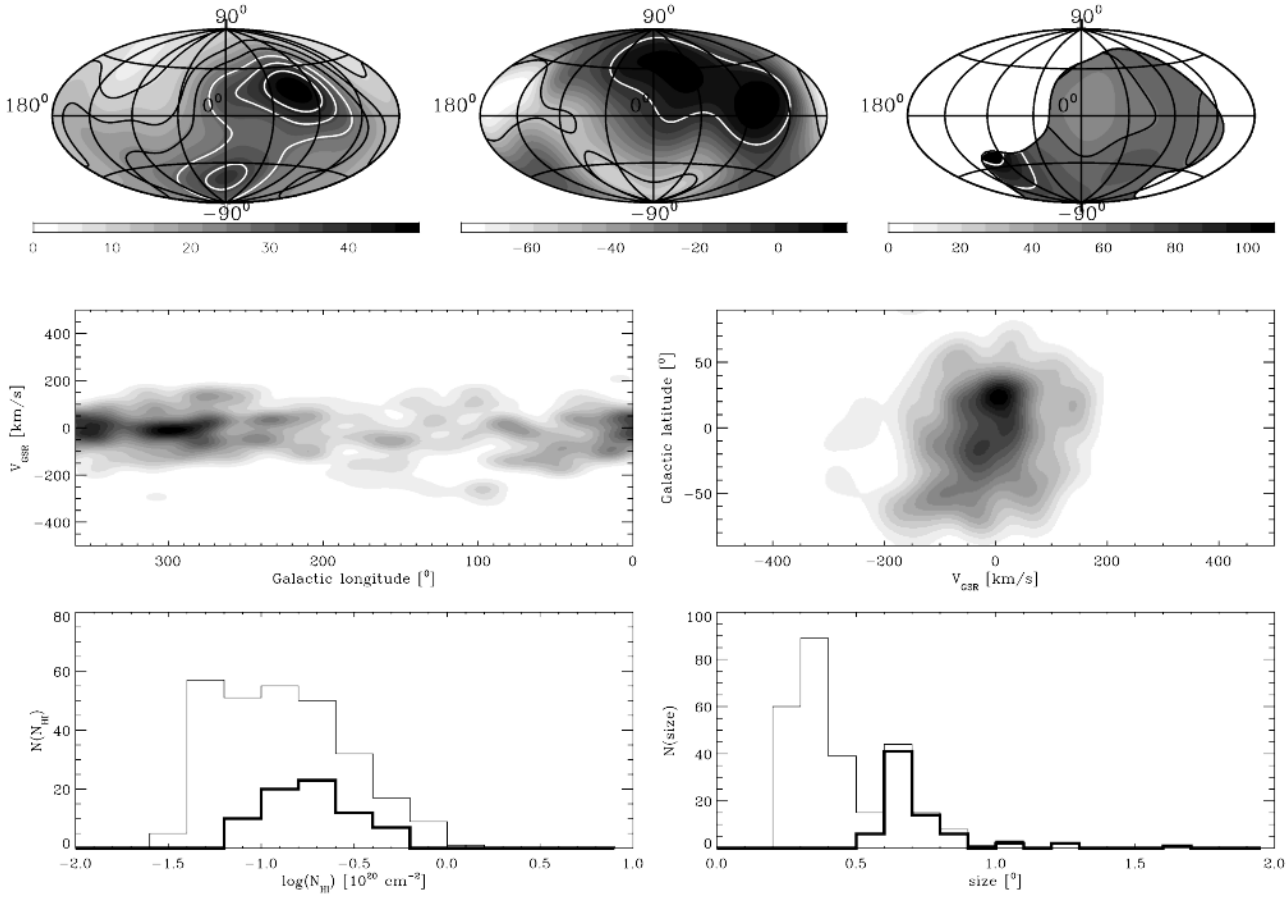

Fig. 19. Overview of the spatial and kinematic properties of one of the best fitting Local Group models before including the effects of foreground obscuration and SGP exclusion. The simulation, model #9 in Table 4, is shown in Fig. 17 after applying these effects. The panels provide the same information as the panels in Fig. 9 for the observed data.

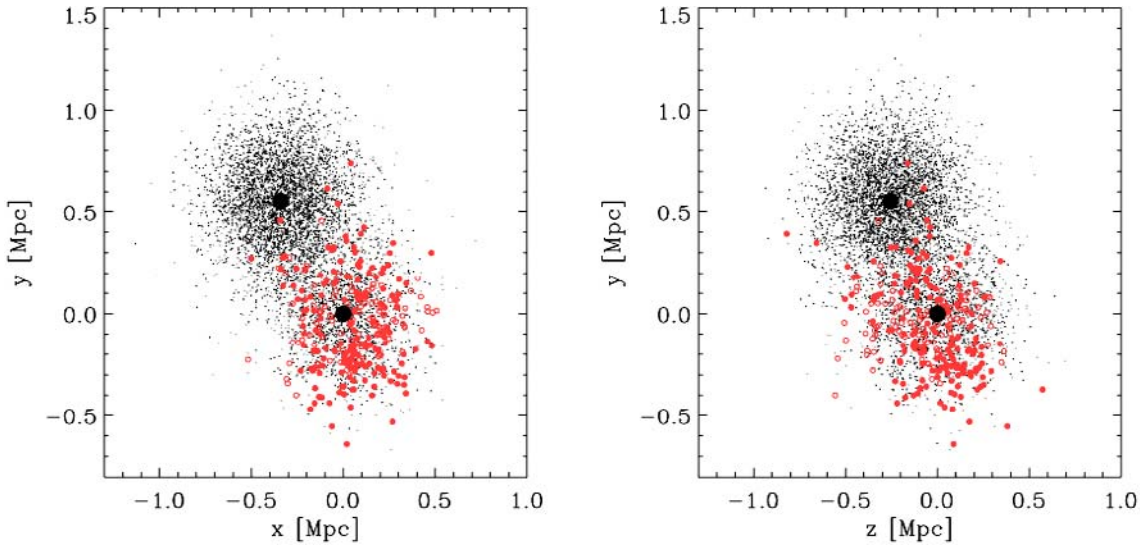

Fig. 20. Three–dimensional distribution of synthetic clouds in the model #9 simulation of a CHVC population in the Local Group. The Galaxy and M 31 are indicated with the large black dots, with the Galaxy at $(x, y, z) = (0, 0, 0)$. The axes are labeled in units of Mpc. The smaller circles indicate all of the objects in the model, whose parameters are given in Table 4. Not all of the clouds survive the simulated environment, and not all of those that do survive would be detected in the LDS and HIPASS observations. The filled black circles indicated those input clouds that are destroyed by tidal and ram–pressure stripping influences of M 31 and the Galaxy. The filled grey circles indicate clouds that are too faint to be detected by the LDS or by HIPASS, respectively, depending on their declination as viewed from the origin. The open red circles are the objects that are obscured by the foreground Galactic H I. Only the filled red circles would be detected in the combined LDS and HIPASS CHVC sample. (This figure is available in color in electronic form.)

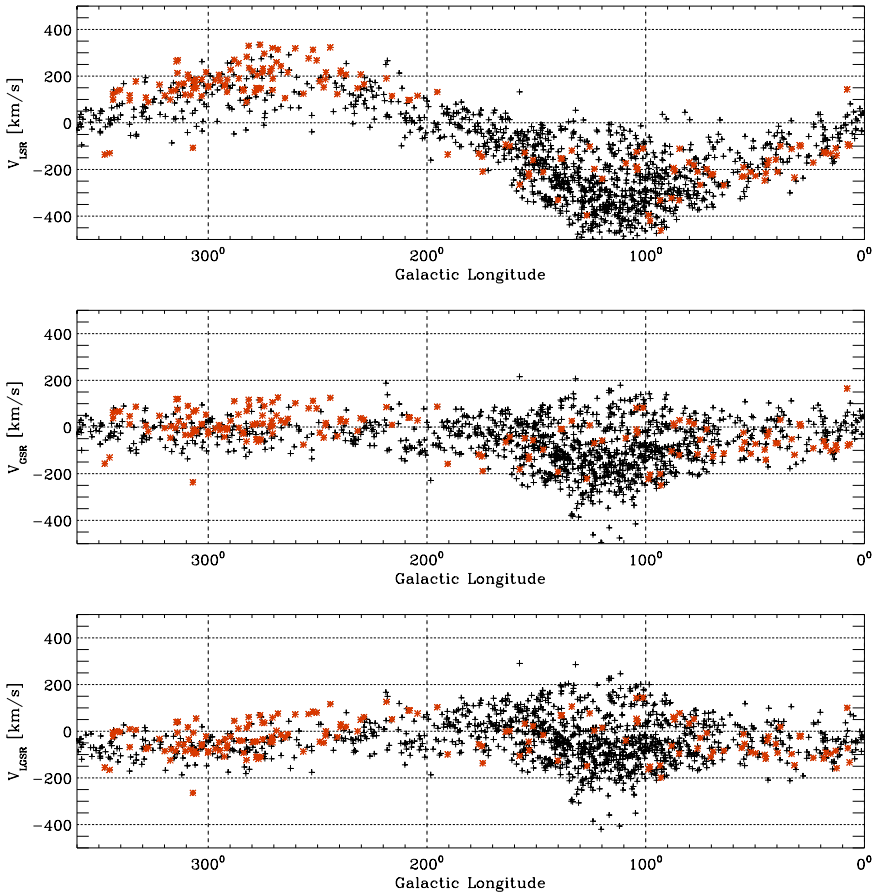

Fig. 21. Velocities plotted against galactic longitude for the ensemble of synthetic clouds corresponding to model #9 of a CHVC population in the Local Group, whose sky deployment is plotted in Fig. 17. The red symbols indicate unobscured clouds which are sufficiently bright to be detected by the Leiden/Dwingeloo or Parkes surveys, depending on the object declination. Black symbols refer to simulated clouds which are either too faint to be detected or obscured. As in the observed velocity, longitude plots of Fig. 6, the kinematic distributions for the simulated situation are indicated for three different kinematic reference frames, namely the LSR (upper), the GSR (middle), and the LGSR (lower panel). (This figure is available in color in electronic form.)

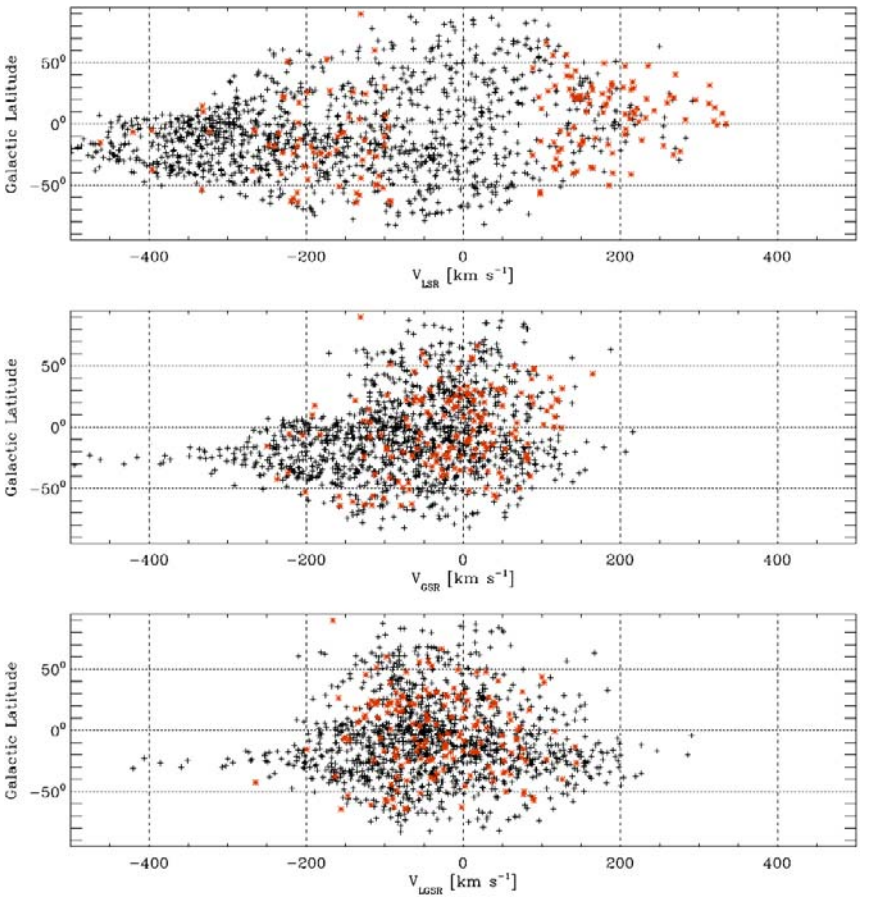

Fig. 22. Velocities plotted against galactic latitude for the ensemble of synthetic clouds corresponding to model #9 of a CHVC population in the Local Group. The kinematic distributions are indicated for three different kinematic reference frames, namely the LSR (upper), the GSR (middle), and the LGSR (lower panel). As in the simulated (l, V) distribution of Fig. 21, red symbols indicate unobscured clouds which are sufficiently bright to be detected by the Leiden/Dwingeloo or Parkes surveys, depending on the object declination, while black symbols refer to simulated clouds which are either too faint to be detected or obscured. The simulated (b, V) plot may be compared with the observed situation plotted in Fig. 7. (This figure is available in color in electronic form.)

Table 2. Average velocity and velocity dispersion for the CHVC ensemble and for the dwarf galaxies in the Local Group, expressed for three different kinematic reference frames. To correct for the difference in sensitivity between the LDS and the HIPASS compilations, the HIPASS CHVCs were weighted by the likelihood that they would be observed in an LDS–like survey. The three values given for the average velocity and for the dispersion for the CHVC ensemble for each reference frame, pertain to an LDS sensitivity 25% lower than the one shown in Fig. 11 of Paper I, to the same sensitivity, and to a sensitivity that is 25% higher, respectively. The Local Group data refer to 27 dwarf galaxies with known radial velocities, from the tabulation of Mateo (1998).

reference frame	CHVCs <velocity> (km s^{-1})	CHVCs dispersion (km s^{-1})	L.G. galaxies <velocity> (km s^{-1})	L.G. galaxies dispersion (km s^{-1})
LSR	−33	253	−57	196
	−45	238		
	−59	240		
GSR	−58	128	−22	104
	−63	128		
	−69	126		
LGSR	−57	114	+4	79
	−60	112		
	−65	110		

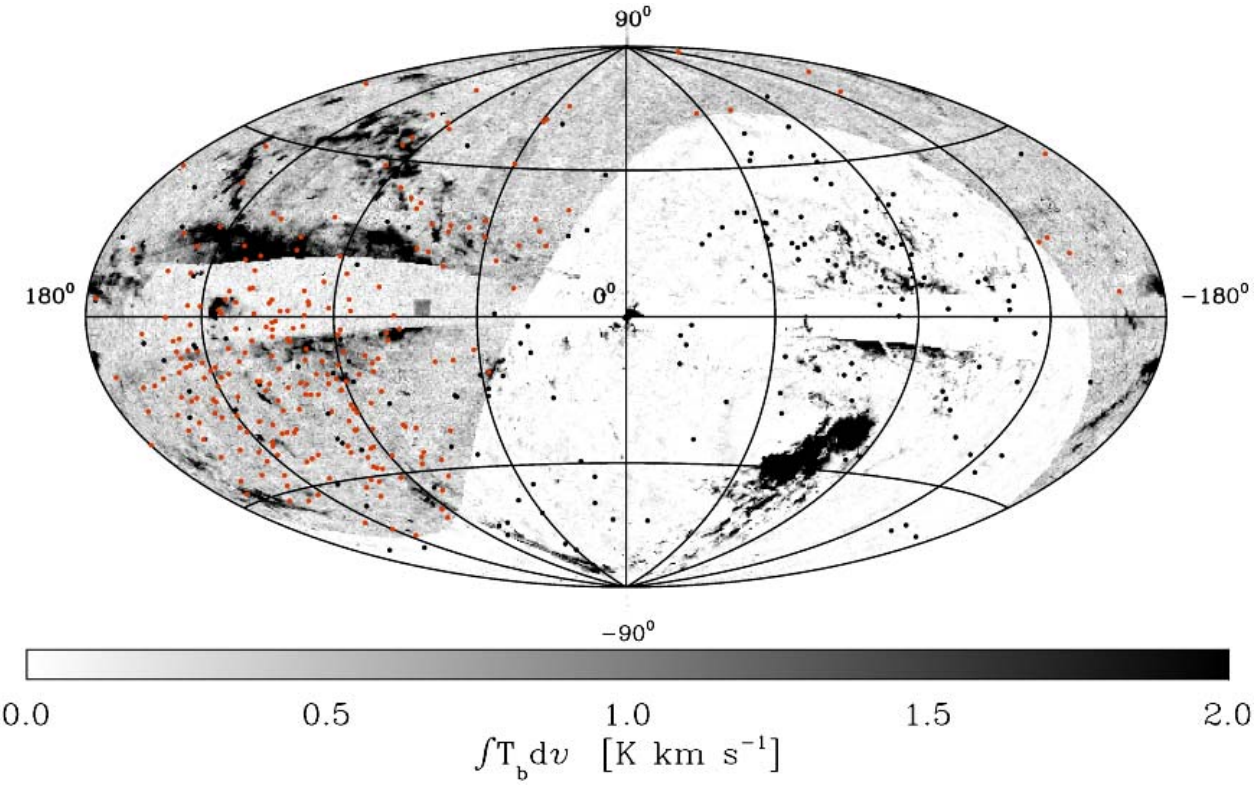

Fig. 23. Predicted distribution on the sky of detected synthetic clouds corresponding to the model #9 simulation of a CHVC population in the Local Group, contrasting LDS and HIPASS sensitivities; the parameters of the simulation are given in Table 4. The black dots correspond to objects that exceed the LDS and HIPASS detection threshold and are not obscured by Galactic H I. The red dots are predicted additional detections if the HIPASS sensitivity were extended to the northern hemisphere. The superposed grey–scale image shows, as in Fig. 5, the observed H I column depths, following from an integration of observed temperatures over velocities ranging from $V_{\rm LSR}$ = −450 km s^{-1} to +400 km s^{-1}, but excluding all gas with $V_{\rm DEV}$ < 70 km s^{-1}. The boundary between the LDS regime at $\delta > 0°$ and the HIPASS regime at lower declinations is evident in the grey–scale image. A much higher CHVC concentration, relative to that currently observed in Fig. 5, is predicted in the direction of the Local Group barycenter at this increased sensitivity. (This figure is available in color in electronic form.)

Way and M 31 and their satellites, Blitz et al. described the dynamics of the Local Group in a straightforward manner. Driven by their mutual gravity and the tidal field of the neighboring galaxies, the Milky Way and M 31 approach each other on a nearly radial orbit. The motion of the dark matter halos which fill the Local Group was determined by the gravitational attraction of the Milky Way and M 31, and the tidal field of the neighboring galaxies. All halos which ever got closer than a comoving distance of 100 kpc from the Milky Way or M 31 center were removed from the sample. Blitz et al. describe how

their simulations account for several aspects of the HVC observations. We follow here the modeling approach of Blitz et al., but judge the results of our simulations against the properties of the CHVC sample, viewing the simulated data *as if it were observed* with the LDS and HIPASS surveys.

4.1. Model description

We use a test particle approach similar to that used by Blitz et al. (1999) to derive the kinematic history of particles as a function of their current position within the Local Group, but combine this with an assumed functional form (rather than simply a uniform initial space density) to describe the number density distribution of the test particles. The density function contains a free parameter which sets the degree of concentration of the clouds around the Milky Way and M 31. By determining a best fit of the models we are able to constrain the values of this concentration parameter, and thereby constrain the distance to the CHVCs. The fits depend upon the derived velocity field and the H I properties of the clouds.

The density fields which we use are a sum of two Gaussian distributions, centered on the Galaxy and M 31, respectively. As a free parameter we use the radial dispersion of these distributions. This free parameter has the same value for both the concentration around the Galaxy and that around M 31. The ratio of the central densities of the distributions at M 31 and the Galaxy must also be specified. We set this ratio equal to the mass ratio of the two galaxies. The Gaussian dispersions which are used in the models range from 100 kpc to 2 Mpc; i.e. the distributions range from very tightly concentrated around the galaxies to an almost homogeneous filling of the Local Group.

The CHVC kinematics are simulated by tracking the motions of small test particles within the gravitational field of the Milky Way, the M 31 system, and the nearby galaxies. Both the description of the tidal field that is produced by the nearby galaxies, and the properties of the Galaxy–M 31 orbit, are taken from the analysis of Raychaudhury & Lynden–Bell (1989), who studied the influence of the tidal field on the motion of the Galaxy and M 31, deriving the dipole tidal field from a catalog of galaxies compiled by Kraan–Korteweg (1986). The motions of the Galaxy and M 31 are determined in a simulation. In this simulation M 31 and the Galaxy are released a short time after the Big Bang. The initial conditions are tuned in such a way that the relative radial velocity and position correspond with the values currently measured.

We track not only the motions of M 31 and the Galaxy, but also the motions of a million test particles. The test particles are, together with M 31 and the Milky Way, released a short time after the Big Bang with a velocity equal to that of the Hubble flow. Initially, the test particles homogenously fill a sphere with a comoving radius of 2.5 Mpc. Their motions are completely governed by the gravitational field of M 31 and the Milky Way and by the tidal field of the nearby galaxies. The result of the simulation at the present age of the Universe is used to define the kinematic history as a function of current 3–D position within the Local Group for our simulated CHVC populations. For every 3–D position where an object is to be placed by our assumed density distribution, we simply assign the kinematic history from the test particle in the kinematic simulation which ended nearest to that 3–D position. The most important aspects of the kinematic history are merely the final space velocity vector as well as the parameters of the closest approach of the test particle to M 31 and the Milky Way, where the effects of ram pressure and tidal stripping will be assessed.

The parameters which determine the outcome of the simulation are the Hubble constant, H, the average density of the Universe, Ω_0, the total mass of the Local Group, $M_{\rm LG}$, ($=M_{\rm M\,31}+M_{\rm MW}$), and the mass–to–light ratio of the nearby galaxies, which make up the tidal field. The Hubble constant and the average density of the Universe not only set the age of the Universe, but also the initial velocities of the test particles. Further evolution is independent of these parameters. The evolution is set by the values of the tidal field and the masses of M 31 and the Galaxy. Values for all these parameters were taken from Raychaudhury and Lynden–Bell (1989), namely: $H = 50$ km s^{-1}, $M_{\rm LG} = 4.3 \times 10^{12}$ $M_\odot$, a mass–to–light ratio of 60, $\Omega_0 = 1$, and $M_{\rm M\,31}/M_{\rm MW} = 2$. Whereas the mutual gravitational attraction between the Milky Way and M 31 is described by a point–mass potential, the gravitational attraction of these galaxies on the test particles is described by an isochrone potential of the form

$$\Phi_{\rm iso}(r) = -\frac{G\,M}{r_0 + \sqrt{{r_0}^2 + r^2}}, \tag{4}$$

where M is the total mass of the galaxy and r_0 is a characteristic radius; r_0 is set such that the rotation velocity as derived from the potential equals the measured one at the edge of the unwarped H I disk, i.e. $V_{\rm circ}^{\rm MW}(12\ {\rm kpc}) = 220$ km s^{-1} and $V_{\rm circ}^{\rm M\,31}(16\ {\rm kpc}) = 250$ km s^{-1}. Figure 11 shows the average velocity field superposed on density contours for a Gaussian distribution of the test particles, characterized by a dispersion of 200 kpc. The ellipsoidal turn–around surface of the Local Group can be seen where the velocity vectors approach zero length at radii near 1.2 Mpc. The velocity field is approximately radial at large distances from both M 31 and the Galaxy, but becomes more complex at smaller radii.

Before we can simulate the way in which a Local Group population of clouds would be observed by a HIPASS– or LDS–like survey, we have to set the H I properties of the test clouds. To do so, we assume that the H I clouds are isothermal gas spheres, with each such cloud located inside a dark–matter halo. Given the temperature of the gas and the potential in which it resides, the density profile follows from the relation

$$n(r) = n_0 \cdot \exp\left(-\frac{m_{\rm HI}}{kT_{\rm eff}}\,[\Phi(r) - \Phi(0)]\right), \tag{5}$$

where $m_{\rm HI}$ is the mass of the hydrogen atom, $\Phi(r)$ is the potential at a distance r from the cloud center, and $T_{\rm eff}$ is an effective gas temperature. Since in addition to the thermal pressure there is also rotational support of a gas cloud against the gravitational attraction of the dark–matter halo, an effective temperature is used which incorporates both processes. In general, the

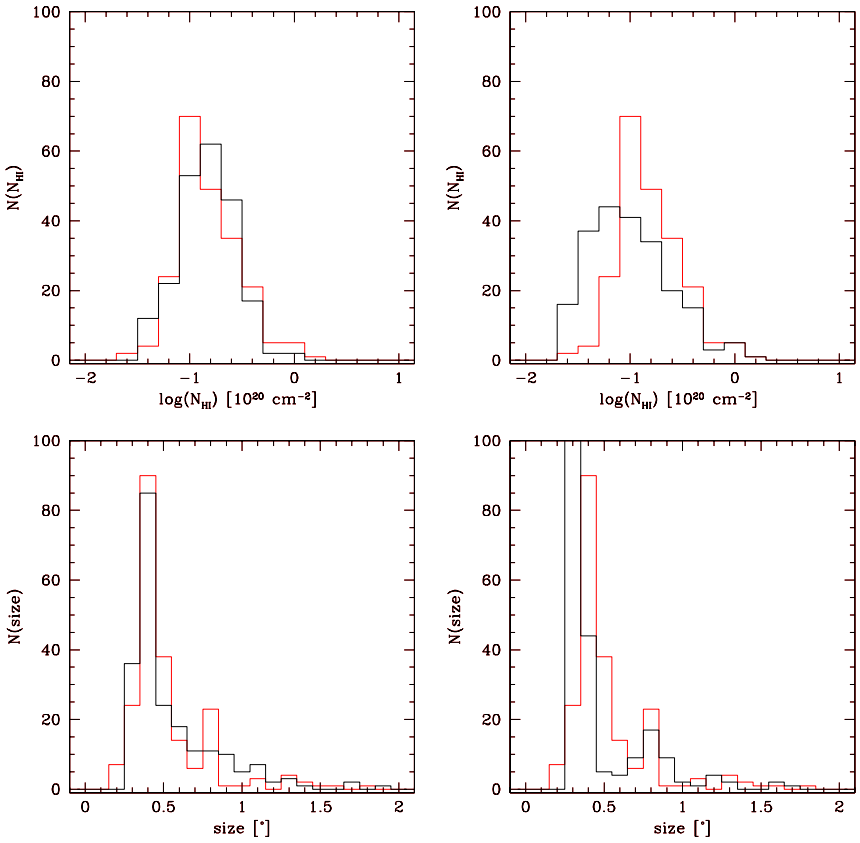

Fig. 24. Demonstration of the quality of the fits of the Galactic Halo models discussed in Sect. 5. The upper panels show the column–density fits; the lower panels show the size fits. The panels on the left represent one of the better fits, characterized by $\chi^2(\mathrm{size}) = 1.7$ and $\chi^2(N_{\mathrm{HI}}) = 0.7$; the panels on the right show one of the poorer fits in the acceptable category, characterized by $\chi^2(\mathrm{size}) = 4.9$ and $\chi^2(N_{\mathrm{HI}}) = 4.9$. The observed distributions are indicated by the red histograms, against which the simulations are judged. (This figure is available in color in electronic form.)

average energy of an atom equals $\frac{1}{2}kT$ per motional degree of freedom, so we have defined the effective temperature such that

$$\frac{3}{2}kT_{\mathrm{eff}} = \frac{3}{2}kT_{\mathrm{kin}} + \frac{1}{2}m_{\mathrm{HI}}V_{\mathrm{circ}}^2, \tag{6}$$

where T_{kin} is the gas kinetic temperature, taken to be 8000 K, and V_{circ} is a characteristic rotation velocity.

The description of the gravitational potential of the dark matter halo follows that of Burkert (1995), who was able to fit a *universal* function to the rotation curves of four different dwarf galaxies. The shape of the function is completely set by the amount of dark matter in the core, M_0. The potential, which is derived from the rotation curve, has the form

$$\begin{aligned}\Phi(r) - \Phi(0) \;=\; & -\pi\, G\, \rho_0\, r_0^2 \left\{ 2\left(1 + \frac{r_0}{r}\right) \cdot \ln\left(1 + r/r_0\right) \right. \\ & -2\left(1 + \frac{r_0}{r}\right) \cdot \arctan\left(r/r_0\right) \\ & \left. -\left(1 - \frac{r_0}{r}\right) \cdot \ln\left(1 + (r/r_0)^2\right) \right\},\end{aligned}$$

where the core radius, r_0, and the central density, ρ_0, are set by the relations

$$r_0 \;=\; 3.07 \left(\frac{M_0}{10^9\ M_\odot}\right)^{3/7} \ \mathrm{kpc}$$

and

$$\rho_0 \;=\; 1.46 \times 10^{-24} \left(\frac{M_0}{10^9\ M_\odot}\right)^{-2/7} \ \mathrm{g\ cm^{-3}}.$$

The circular–velocity rotation curve has a maximum value

$$V_{\mathrm{circ}}^{\mathrm{max}} = 48.7 \left(\frac{M_0}{10^9\ M_\odot}\right)^{(2/7)} \ \mathrm{km\ s^{-1}}. \tag{7}$$

We use $V_{\mathrm{circ}}^{\mathrm{max}}$ as a parameter for V_{circ} in Eq. (6). Because the total mass corresponding to the given potential is infinite, the dark matter mass is characterised either by the core mass, M_0, or by the virialized mass of the halo, M_{vir}. We adopt a total dark–matter mass of M_{vir} for each object. According to Burkert (1995), these are related by $M_{\mathrm{vir}} = 5.8\ M_0$.

Although we could use Eq. (5) directly to determine the predicted 21–cm images of a CHVC given an H I mass, we instead chose to approximate the corresponding column–density distribution by a Gaussian, in order to enable faster evaluation of the simulation. Two parameters specify the Gaussian, namely the central density, n_0, and the *FWHM*, derived as follows. The volume–density distribution given by Eq. (5), can be closely approximated with an exponential form with a matched scale–length, h_{e}, defined by $n(h_{\mathrm{e}}) = n(0)/e$. The column density distribution can then be expressed in an analytic form, containing a modified Bessel function of order 1 (e.g. Burton et al. 2001). This analytic representation of the column–density distribution is then approximated by a Gaussian of the same halfwidth from, $FWHM = 2.543 h_{\mathrm{e}}$. Knowing the mass of the H I gas cloud and its *FWHM*, the central density of the Gaussian can be determined.

To get the amount of H I mass in the cloud, we adopt the relations between the dark–matter mass and baryonic mass for galaxies. For normal, massive galaxies there is approximately ten times as much dark matter as there is baryonic matter. Chiu

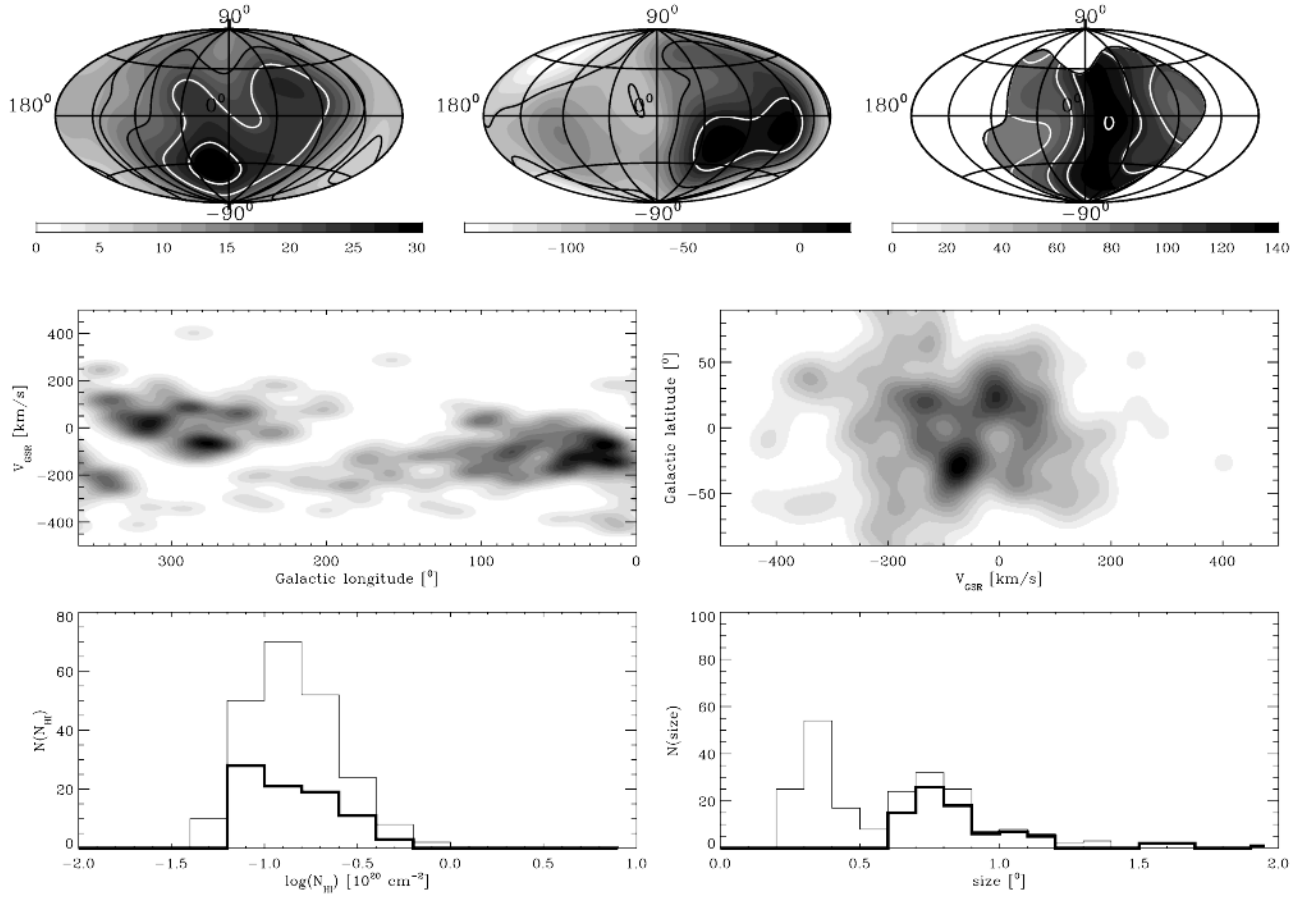

Fig. 25. Summary of the simulated spatial and kinematic properties of the CHVC ensemble, for one of the better fits of the empirical Galactic Halo model described in Sect. 5. The panels give the properties of the simulation in the same way as the panels in Fig. 9 describe the observed data. This Galactic Halo simulation is determined by the following parameters: $M_0 = 10^4\ M_\odot$, $n_0 = 3 \times 10^2\ \mathrm{cm}^{-3}$, $\beta = -2.0$, and $\sigma_\mathrm{d} = 30$ kpc. The quality of the fit is described by $\chi^2(\mathrm{size}) = 2.3$ and $\chi^2(N_\mathrm{HI}) = 2.6$. The thick–line histograms indicate the LDS (northern hemisphere) contributions to the total detections.

et al. (2001) show that this ratio depends on the total mass. Whereas the mass spectrum of the dark–matter halos in their simulation has the form $n(M_\mathrm{dark}) \propto M_\mathrm{dark}^{-2}$, the baryonic mass spectrum has the form $n(M_\mathrm{HI}) \propto M_\mathrm{HI}^{-1.6}$. The difference in slope is due to the ionizing extragalactic radiation field. The lowest mass halos are simply unable to retain their ionized baryonic envelopes, which have a kinetic temperature of 10^4 K. The slopes of both the baryonic and the dark–matter distributions completely determine the mass dependency of the ratio between dark matter and baryonic matter. Furthermore, given the fact that the ratio equals 10 for objects with a baryonic mass of $10^9\ M_\odot$, the ratio is set for all masses. Although the simulation of Chiu et al. gives a value of −1.6 for the baryonic mass spectrum slope, we explore a range of values for the H I mass spectrum. The most appropriate value is then obtained by fitting the models to the observations.

For the sake of simplicity, we assume that the baryonic mass of each simulated cloud is entirely in the form of H I. In fact, a significant mass fraction will be in the form of ionized gas. It is likely that the mass fraction of ionized gas will increase toward lower masses such that below some limiting mass the objects would be fully ionized. A realistic treatment of the ionized mass fraction was deemed beyond the scope of this study. However, we do comment further on the implications of this simplifying assumption where appropriate.

The definitions of the velocity and density fields of the test objects in the Local Group, together with their H I properties, resulted in simulated CHVC populations which could be sampled with the observational parameters of an LDS– or HIPASS–like survey. The free parameters, defined above, were allowed to take the following values:

- The Gaussian dispersion of the density distributions centered on the Galaxy and M 31 can range from 100 kpc to 2 Mpc;
- The slope of the H I mass spectrum, β, not only sets the number ratio of the less–massive with respect to the more–massive objects, it also determines the dark–to–baryonic mass ratios. The slope is allowed to range over the values −2.0, −1.9, −1.8, −1.7, −1.6, −1.4, −1.2, −1.0;
- M_1 is the highest H I mass which is allowed for clouds in the simulations. The logarithm of this mass is allowed the values 6.0, 6.5, ..., 9.0. It was found necessary to introduce this upper mass cut–off since otherwise high column densities $N_\mathrm{HI} \sim 10^{21}\,\mathrm{cm}^{-2}$ were predicted, such as observed in actively star-forming galaxies, but unlike what is found in the CHVC population.

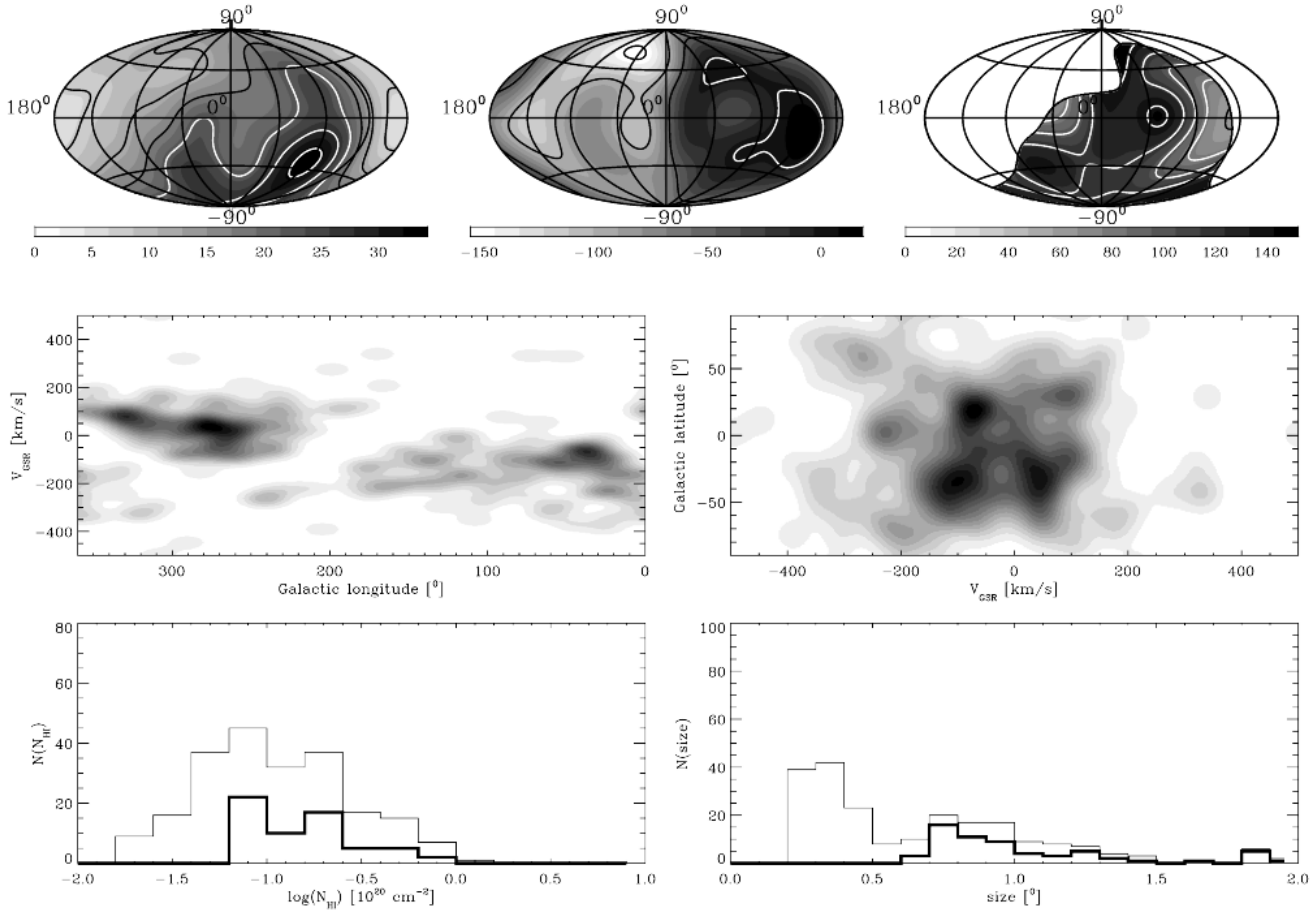

Fig. 26. Summary of the simulated spatial and kinematic properties of the CHVC ensemble, for one of the better fits of the empirical Galactic Halo model described in Sect. 5. The panels give the properties of the simulation in the same way as the panels in Fig. 9 describe the observed data. This Halo simulation is determined by the following parameters: $M_0 = 10^5\ M_\odot$, $n_0 = 3 \times 10^{-3}$ cm^{-3}, $\beta = -1.4$, and $\sigma_d = 200$ kpc. The quality of the fit is described by $\chi^2(\text{size}) = 2.9$ and $\chi^2(N_{\rm HI}) = 2.5$. The thick–line histograms indicate the LDS (northern hemisphere) contributions to the total detections. Although this Halo model is fundamentally different from the Local Group models, the characteristic distance of the simulated CHVCs is similar.

Figure 12 shows the basic cloud properties as a functions of H I mass. As indicated above, the dark–matter fraction as function of mass is determined by β, the slope of the H I mass spectrum, so three curves are shown in each panel, corresponding to $\beta = -1.2$, -1.6, and -2.0, respectively. The typical object size and internal velocity dispersion increases only slowly with H I mass, from about 1.5 to 4 kpc, and 10 to 20 km s^{-1}, respectively, between $M_{\rm HI} = 10^5$ and $10^8\ M_\odot$. The central H I volume density varies much more dramatically with H I mass, as does the peak column density. Note that the peak column densities of simulated clouds only exceed $N_{\rm HI} > 10^{19}$ cm^{-2} for $M_{\rm HI} > 10^{5.5}\ M_\odot$ and β in the range -1.6–-2.0. It is critical that peak column densities of this order are achieved in long-lived objects, since this is required for self-shielding from the extragalactic ionizing radiation field (e.g. Maloney 1993; Corbelli & Salpeter 1993).

In order to compare the simulation results with the observational data in the most effective way, and thereby constrain the model parameters, we created a single CHVC catalog from the HIPASS and LDS ones. Thirty-eight CHVCs at $\delta \geq 0°$ were extracted from the de Heij et al. (2002) LDS catalog, and 179 at $\delta < 0°$ from the Putman et al. (2002) HIPASS one. A large concentration of faint sources (Group 1 noted above) with an exceptionally high velocity dispersion is detected toward the Galactic south pole. Because this overdensity may well be related to the nearby Sculptor group of galaxies (see Putman et al. 2002), the 53 CHVCs at $b < -65°$ were excluded from comparison with the simulations.

A simulation was run for each set of model parameters. We chose a position for each object, in agreement with the spatial density distribution of the ensemble, but otherwise randomly. The velocity is given by the velocity field described above. The H I mass of the test cloud is randomly set in agreement with the given power–law mass distribution between the specified upper mass limit and a lower mass limit described below. The physical size and linewidth of each object follow from the choice of β. Once all these parameters were set, we determined the observed peak column density and angular size. Objects in the northern hemisphere were convolved with a beam appropriate to the LDS, while those at $\delta < 0°$ were convolved with the HIPASS beam. Simulated objects were considered detected if the peak brightness temperature exceeded the

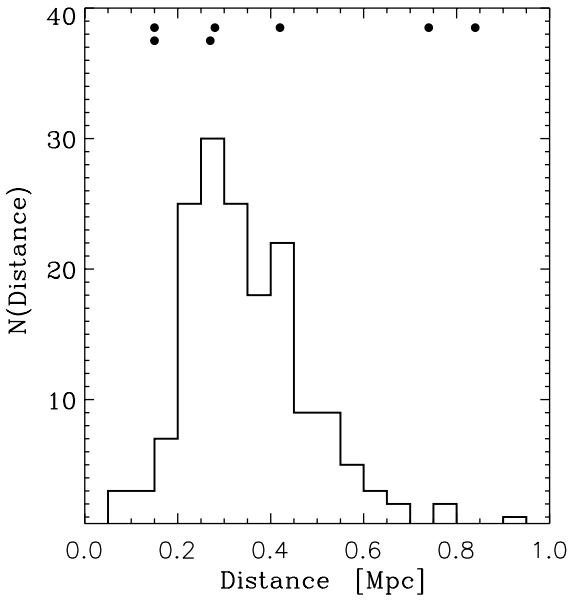

Fig. 27. Histogram of object distances for one of the best-fitting Local Group models. The detected objects in model #9 of Table 4 are plotted in the histogram. A broad peak in the distribution extends from about 200 to 450 kpc, with outliers as far as 1 Mpc. The filled circles along the top of the figure are the distance estimates for individual CHVCs of Braun & Burton (2000) and Burton et al. (2001), based on several different considerations. While few in number, they appear consistent with this distribution.

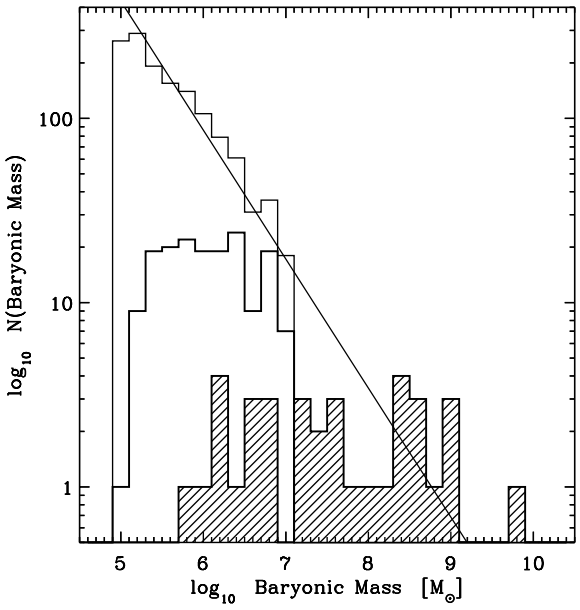

Fig. 28. Comparison of a model Local Group CHVC population with the population of Local Group galaxies. The distribution of H I masses of one of our best–fitting Local Group models, model #9 of Table 4, is plotted as a thin–line histogram after accounting for ram–pressure and tidal stripping and as a thick line after also accounting for Galactic obscuration and the finite sensitivities of the LDS and HIPASS observations. The Local Group galaxies (excluding M 31 and the Galaxy) tabulated by Mateo (1998) are plotted as the hatched histogram after summing the H I mass with the stellar mass assuming $M/L_B = 3\,M_\odot/L_\odot$. The diagonal line has the slope of the H I power–law mass function, $\beta = -1.7$.

detection threshold of the relevant survey, i.e. the LDS for objects at $\delta > 0°$, and HIPASS otherwise. Furthermore, in order for a test object to be retained as detected its deviation velocity was required to exceed 70 km s^{-1} in the LSR frame, and its Galactic latitude to be above $b = -65°$ (for consistency with the exclusion of Group 1 from our CHVC sample noted above). In addition, as we describe below, each simulated cloud should be stable against both tidal disruption and ram–pressure stripping by the Milky Way and M 31. We continued simulating additional objects following this prescription until the number of detected model clouds was equal to the number of CHVCs in our observed all–sky sample.

Before carrying out each simulation with a power–law distribution of H I masses we began by determining an effective lower H I mass limit, M_0, to the objects that should be considered. This was necessary to avoid devoting most of the calculation effort to objects too faint to be detected in any case. As a first guess we took $M_0 = 0.5M_1$. A sub-sample of twenty objects in the mass range M_0–M_1 was simulated which were deemed stable to both disruption and stripping and were detectable with the relevant survey parameters. Generating twenty detectable objects typically required evaluating of order 500 test objects. Given the total number of test objects needed to generate this observable sub–sample and the slope of the H I mass distribution function, it is possible to extrapolate the number of required test objects in other intervals of H I mass belonging to this same distribution. The predicted number of test objects in the interval $0.67M_0$ to M_0 was simulated. If at least one of these was deemed detectable, then the lower H I mass limit was replaced with $0.67M_0$ and the procedure outlined above was repeated. This process continued until no detectable object was found in the mass interval $0.67M_0$ to M_0. Tests carried out with better number statistics, involving a sub–sample size of 180 objects and requiring a minimum of nine detections in the lowest mass interval, demonstrated that this procedure was robust.

Figure 13 shows the distance out to which simulated CHVCs of a given H I mass can be detected with the HIPASS survey. Both the H I linewidth and spatial *FWHM* are dependent on the dark–matter fraction, as illustrated in Fig. 12, so separate curves are shown for $\beta = -1.2$, -1.6, and -2.0. A limiting case is provided by $\beta = -1.2$ which is extremely dark–matter dominated for low H I mass. In this case the objects are so spatially extended (about 5 kpc *FWHM*) and have such a high linewidth (about 60 km s^{-1} *FWHM*) that they fall below the HIPASS detection threshold for $\log(M_{\rm HI}) < \sim 6.4$. More plausible linewidths and spatial *FWHM* follow for $\beta = -1.6$ and -2.0. Such objects are sufficiently concentrated that they can still be detected, even when highly resolved in the HIPASS data.

The clouds are regarded stable against ram–pressure stripping if the gas pressure at the center of the cloud exceeds the

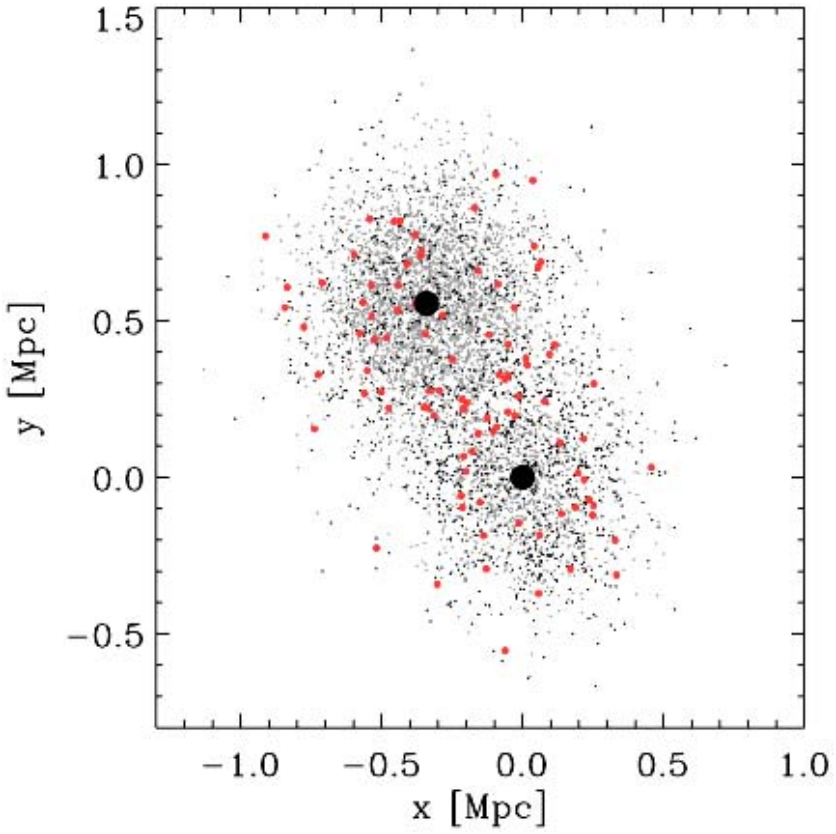

Fig. 29. External appearance of a model Local Group CHVC population. The spatial distribution of one of our best–fitting Local Group models, namely model #9 of Table 4, is shown projected onto a plane as in Fig. 20. The grey dots correspond to objects which have been disrupted by ram–pressure or tidal stripping during a close passage. The red and black dots correspond to are objects which should survive these processes, with the color of the dot distinquishing objects by H I mass. The red dots indicate clouds more massive than $M_{\rm HI} = 3 \times 10^6\,M_\odot$; the black dots indicate CHVCs falling below this mass limit. (This figure is available in color in electronic form.)

ram pressure, $P_{\rm ram} = n_{\rm halo} \cdot V^2$, for a cloud moving with velocity V through a gaseous halo with density $n_{\rm halo}$. Because both the gaseous halo density and the cloud velocity are the highest if the distance of the cloud to the galaxy is the smallest, the stability against ram–pressure stripping was evaluated at closest approach. We therefore kept track of the closest approach of each test–particle to the Galaxy and to M 31, while simulating the velocity field of the Local Group. We used a density profile for the Galactic halo which is an adaptation of the model of Pietz et al. (1998), derived to explain the diffuse soft X–ray emission as observed by ROSAT. Whereas their model is flattened towards the Galactic plane, we simply use a spherical density distribution, in which the radial profile is equal to the Galactic plane density profile of Pietz et al. The density at a distance r from the Galactic center is given by

$$n(r) = n_0 \cdot \left(\frac{\cosh(r_\odot/h)}{\cosh(r/h)} \right)^2, \qquad (8)$$

where $n_0 = 0.0013\,{\rm cm}^{-3}$ is the central density, $h = 12.5\,{\rm kpc}$ is the scalelength of the distribution, and $r_\odot = 8.5\,{\rm kpc}$ is the radius of the solar orbit around the Galactic center. According to this model, the total mass in the Galactic halo is $1.5 \times 10^9\,M_\odot$. To describe the halo around M 31, we use the same expression and the same parameter values except for n_0, for which we use a value twice the Galactic one. Figure 14 shows an example of the calculated distance at which a cloud of a particular H I mass will be stripped. The clouds in this example are assumed to have a relative velocity of 200 km s^{-1} with respect to the Galactic halo.

A cloud will be tidally disrupted if the gravitational tidal field of either the Galaxy or M 31 exceeds the self–gravity of the cloud. We consider a cloud stable if

$$\frac{M_{\rm dark}}{\sigma^2} \geq \left| \frac{{\rm d}^2}{{\rm d}r^2} \Phi_{\rm iso}(r) \right| \cdot \sigma, \qquad (9)$$

where σ is the spatial dispersion of the Gaussian describing the H I distribution in the cloud, $M_{\rm dark}(r \leq \sigma)$ is the core mass of the dark matter halo, and $|{\rm d}^2\Phi_{\rm iso}(r)/{\rm d}r^2|$ is the tidal force of either the Galaxy or M 31. Solving the equation for r shows that only the least massive clouds with the lowest dark–matter fractions are likely to suffer from tidal disruption. If the slope of the H I mass distribution is as steep as -2.0, then clouds with an H I mass less than $10^5\,M_\odot$ are tidally disrupted at distances of about 60 kpc, as shown in Fig. 15. For $M_{\rm HI} > 2 \times 10^5\,M_\odot$, or $\beta > -2$, the clouds are stable. Changing the radius at which Eq. (9) is evaluated from 1σ to 2σ, does not dramatically change this result.

4.2. Results of the Local Group simulations

Before searching for a global best fit, we determined the range of parameter values over which at least a moderately good representation of the observed data was possible with the simulated data. To quantify the degree of agreement between the simulated size–, column–density and velocity–*FWHM* distributions with the observations, we used a χ^2–test taken from Sect. 14.3 of *Numerical Recipes* (Press et al. 1993). The size–, column–density, and velocity–*FWHM* distributions of a simulation were considered reasonable if $\chi^2({\rm size}) < 3, \chi^2(N_{\rm HI}) < 5$,

and $\chi^2(FWHM) < 5$. The incorporation of the spatial and kinematic information was done by comparing the modeled (l, b), $(l, V_{\rm GSR})$, and $(V_{\rm GSR}, b)$ distributions with those observed. We used the two-dimensional K–S test described in Sect. 14.7 of *Numerical Recipes* to make this comparison. The fits were considered acceptable if $\tilde{\chi}^2(l, b)$, $\tilde{\chi}^2(l, V_{\rm GSR})$, and $\tilde{\chi}^2(V_{\rm GSR}, b)$ where all less than 0.3.

Table 3 shows which part of the parameter space produces moderately good fits. The best fits have a Gaussian dispersion between 150 and 250 kpc, an upper H I mass cut-off between $10^{6.5}$ and $10^{8.0}$ $M_\odot$ and a slope of the H I mass distribution of -1.7 to -1.9.

Each simulation contains a relatively small number of detectable objects, namely the same number of objects as in our all–sky CHVC catalog. Therefore the χ^2 values are prone to shot–noise. By performing a larger number of simulations for a specific combination of free parameters, we are able to determine a more representative value of χ^2 for each model. The most promising combinations of parameter values, i.e. the entries in Table 3, were repeated 35 times to reduce the shot–noise, and the average results and their dispersions are shown in Table 4. The range of resulting fit quality due purely to this shot–noise is illustrated in Fig. 16, which shows model data with the highest and lowest χ^2 values from a sequence of 35 simulations.

The best overall fits are fairly well–constrained to lie between $\sigma_{\rm d} = 150$ and 200 kpc, with an upper H I mass cut–off of about 10^7 to $10^{7.5}$ $M_\odot$ and a slope of the H I mass distribution of -1.7 to -1.8. Comparison with Fig. 12 suggests that populations of these types have sufficiently high peak H I column densities that they can provide self-shielding to the extragalactic ionizing radiation field for $M_{\rm HI} > 10^{5.5}$ $M_\odot$. The results of simulations #9 and #3 from Table 4 are shown in Figs. 17 and 18, respectively. A single instance of each simulation has been used in the subsequent figures that had χ^2 values consistent with the ensemble average.

Both of these Local Group simulations succeed reasonably well in reproducing the observed kinematic and population characteristics of the CHVC sample as summarized in Fig. 9. The CHVC concentrations, named Groups 2, 3, and 4 above, while not reproduced in detail, have counterparts in the simulations which arise from the combination of Gaussian density distributions centered on the Galaxy and M 31, together with the Local Group velocity field, population decimation by disruption effects, and the foreground H I obscuration. A notable success of these simulations is their good reproduction of the smoothed velocity field, including both the numerical values and the location of minima and maxima.

One aspect of the observed CHVC distributions which can not be reproduced accurately by our simulations is the distribution of observed linewidth. The model objects are assumed to contain only the warm component of H I with a minimum linewidth corresponding to a 8000 K gas. The profiles are then further broadened by the contribution of rotation as indicated in Eq. (6). The actual objects are known to have cool core components (e.g. Braun & Burton 2001; Burton et al. 2001) which can contribute a significant fraction of the H I mass and consequently lead to narrower observed line profiles. This shortcoming of the model distributions is illustrated in the central panel of Fig. 16. The narrow–linewidth tail of the observed distributions can never be reproduced by the models. The best–fitting models can only succeed in reproducing the median value and high-velocity tail of the distribution.

In order to better isolate the effect of foreground obscuration from the intrinsic distribution properties of the simulation itself we show the unobscured version of model #9 in Fig. 19. Comparison of Figs. 17 and 19 illustrates how the foreground obscuration from the H I Zone of Avoidance modifies the distribution of object density. The location of apparent object concentrations are shifted and density contrasts are enhanced. The comparison also reveals that the large gradient in the smoothed GSR velocity field is an intrinsic property of the Local Group model and not simply an artifact of the Galactic obscuration. Substantial negative velocities (<-100 km s^{-1}) are predicted in the direction of M 31 (which effectively defines the Local Group barycenter), while slightly positive velocities are predicted in the anti-barycenter direction, just as observed.

A better appreciation of the physical appearance of these Local Group models is provided in Fig. 20, where two perpendicular projections of the model #9 population are displayed. The (x, y) plane in the figure is the extended Galactic plane, with the Galaxy centered at $(x, y) = (0, 0)$ with the positive z axis corresponding to positive b. The intrinsic distribution of objects is an elongated cloud encompassing both the Galaxy and M 31, which is dominated in number by the M 31 concentration. The objects that have at some point in their history approached so closely to either of these galaxies that their H I would not survive the ram–pressure or tidal stripping are indicated by the filled black circles. Cloud disruption appears to have been substantially more important in the M 31 concentration than for the Galaxy. The objects that are too faint to have been detected by the LDS or HIPASS observations, depending on declination, are indicated by grey circles. *The bulk of the M 31 sub–concentration is not detected in our CHVC sample for two reasons*: (1) these objects have a larger average distance than the objects in the Galactic sub–concentration, and (2) the M 31 sub–concentration is located primarily in the northern celestial hemisphere, where the lower LDS sensitivity compromises detection. We will return to this point below.

Those objects which are obscured by the H I distribution of the Galaxy are indicated in Fig. 20 by open red circles. Somewhat counter–intuitively, the consequences of obscuration are not concentrated toward the Galactic plane, but instead occur in the plane perpendicular to the LGSR solar apex direction $(l, b) = (93°, -4°)$. This can be understood by referring back to our discussion in Sect. 2.2.1 and the illustration in Fig. 1. Obscuration from the position– and velocity–dependent H I Zone of Avoidance is most dramatic when the kinematic properties of a population result in overlap with $V_{\rm LSR} = 0$ km s^{-1}, since this can occur over a large solid angle, while the Galactic plane is relatively thin.

The various processes which influence the observed distributions are further quantified in Table 5. Matching the detected sample size of 163 CHVCs above $b = -65°$, required the simulation of some 6300 objects in the case of models #9 and #3. About three quarters of the simulated popula-

Table 3. Tabulation of the range of parameters entering the Local Group models described in Sect. 4. Three free parameters were specified for each simulation, namely the maximum allowed H I mass, M_1 (in units of $M_\odot$), the slope of the H I mass distribution, β, and the Gaussian dispersion of the cloud population, σ_d (in units of kpc). The simulated CHVC populations were subjected to the same observational constraints as pertain to the LDS and HIPASS surveys. The simulated spatial and kinematic deployments, as well as the simulated size–, column density– and velocity–*FWHM* distributions, were compared with those observed. The table shows which Gaussian density dispersions produce acceptable results for each of the combinations of M_1 and β. A field is blank if the simulation returned no acceptable fit for the given parameter combinations. Fits were deemed acceptable if χ^2 size < 3, $\chi^2 N_{HI} < 5$, χ^2 *FWHM* < 5, $\tilde{\chi}^2(l,b) < 0.3$, $\tilde{\chi}^2(l, V_{GSR}) < 0.3$, and $\tilde{\chi}^2(V_{GSR}, b) < 0.3$.

	$M_1 = 10^6\ M_\odot$	$10^{6.5}\ M_\odot$	$10^7\ M_\odot$	$10^{7.5}\ M_\odot$	$10^8\ M_\odot$	$10^{8.5}\ M_\odot$	$10^9\ M_\odot$
$\beta = -1.2$							
-1.4							
-1.6							
-1.7		$\sigma_d = 150 \ldots 200$ kpc	150 … 250	150 … 200	150 … 200		
-1.8			150 … 250	150 … 250	150 … 250		
-1.9				200 … 250	200 … 250		
-2.0							

Table 4. Average chi–square values and their dispersions for the 35 runs which were performed for each model of the Local Group deployment of CHVCs. Each model was specified by the indicated three parameters, namely the Gaussian dispersion of the cloud population, σ_d, the maximum allowed H I mass, M_1, and the slope of the H I mass distribution, β. Multiple runs yielded better estimates of each χ^2, reducing the sensitivity to the relatively small number of objects in each individual simulation. The output of each model was sampled with the observational parameters of the LDS and HIPASS surveys and compared with the observed data.

Model #	σ_d (kpc)	M_1 ($M_\odot$)	β	χ^2(size)	$\chi^2(N_{HI})$	$\chi^2(FWHM)$	$\tilde{\chi}^2(l,b)$	$\tilde{\chi}^2(l, V\mathrm{GSR})$	$\tilde{\chi}^2(V\mathrm{GSR}, b)$
1	150	$10^{6.5}$	−1.7	2.0 ± 0.6	1.9 ± 0.3	4.0 ± 0.4	0.29 ± 0.03	0.25 ± 0.02	0.29 ± 0.03
2	150	$10^{7.0}$	−1.7	2.2 ± 0.5	2.3 ± 0.4	3.5 ± 0.4	0.27 ± 0.03	0.23 ± 0.03	0.28 ± 0.03
3	150	$10^{7.5}$	−1.7	2.6 ± 0.6	2.7 ± 0.4	3.9 ± 0.6	0.25 ± 0.04	0.21 ± 0.03	0.25 ± 0.03
4	150	$10^{8.0}$	−1.7	3.0 ± 0.6	3.0 ± 0.5	3.9 ± 0.5	0.24 ± 0.03	0.21 ± 0.03	0.24 ± 0.02
5	150	$10^{7.0}$	−1.8	2.0 ± 0.5	2.4 ± 0.5	4.5 ± 0.6	0.27 ± 0.04	0.23 ± 0.02	0.28 ± 0.03
6	150	$10^{7.5}$	−1.8	2.4 ± 0.5	2.6 ± 0.5	4.1 ± 0.5	0.25 ± 0.04	0.21 ± 0.03	0.24 ± 0.02
7	150	$10^{8.0}$	−1.8	2.7 ± 0.6	2.7 ± 0.4	4.0 ± 0.6	0.24 ± 0.03	0.21 ± 0.03	0.24 ± 0.03
8	200	$10^{6.5}$	−1.7	2.4 ± 0.5	2.9 ± 0.3	4.9 ± 0.6	0.29 ± 0.04	0.28 ± 0.02	0.30 ± 0.02
9	200	$10^{7.0}$	−1.7	2.3 ± 0.5	2.9 ± 0.3	4.1 ± 0.5	0.28 ± 0.04	0.24 ± 0.02	0.29 ± 0.03
10	200	$10^{7.5}$	−1.7	2.9 ± 0.6	3.0 ± 0.5	4.8 ± 0.7	0.26 ± 0.04	0.22 ± 0.03	0.26 ± 0.03
11	200	$10^{8.0}$	−1.7	3.0 ± 0.5	3.1 ± 0.5	4.9 ± 0.6	0.26 ± 0.04	0.22 ± 0.03	0.25 ± 0.03
12	200	$10^{7.0}$	−1.8	2.2 ± 0.5	3.6 ± 0.5	4.2 ± 0.5	0.28 ± 0.04	0.24 ± 0.03	0.29 ± 0.03
13	200	$10^{7.5}$	−1.8	2.5 ± 0.6	3.7 ± 0.4	3.8 ± 0.5	0.27 ± 0.04	0.22 ± 0.03	0.27 ± 0.03
14	200	$10^{8.0}$	−1.8	2.7 ± 0.5	3.7 ± 0.5	3.6 ± 0.5	0.26 ± 0.04	0.22 ± 0.02	0.26 ± 0.04
15	200	$10^{7.5}$	−1.9	2.3 ± 0.5	4.0 ± 0.5	4.8 ± 0.7	0.26 ± 0.04	0.22 ± 0.03	0.27 ± 0.04
16	200	$10^{8.0}$	−1.9	2.4 ± 0.5	4.0 ± 0.5	4.3 ± 0.8	0.26 ± 0.05	0.22 ± 0.02	0.26 ± 0.04
17	250	$10^{7.0}$	−1.7	2.3 ± 0.6	4.3 ± 0.6	4.8 ± 0.7	0.28 ± 0.04	0.24 ± 0.02	0.29 ± 0.03
18	250	$10^{7.0}$	−1.8	2.2 ± 0.5	5.2 ± 0.6	4.1 ± 0.5	0.26 ± 0.04	0.23 ± 0.02	0.27 ± 0.03
19	250	$10^{7.5}$	−1.8	2.5 ± 0.6	5.1 ± 0.6	3.8 ± 0.5	0.25 ± 0.03	0.22 ± 0.02	0.26 ± 0.03
20	250	$10^{8.0}$	−1.8	2.7 ± 0.4	5.3 ± 0.7	3.6 ± 0.6	0.25 ± 0.04	0.22 ± 0.02	0.25 ± 0.03
21	250	$10^{7.5}$	−1.9	2.3 ± 0.5	5.6 ± 0.6	4.8 ± 0.6	0.26 ± 0.03	0.22 ± 0.02	0.26 ± 0.03
22	250	$10^{8.0}$	−1.9	2.5 ± 0.6	5.6 ± 0.6	4.3 ± 0.6	0.25 ± 0.03	0.22 ± 0.02	0.25 ± 0.03

tions were classified as disrupted due to ram–pressure or tidal stripping; while 80% of the remaining objects were deemed too faint to detect with the LDS (in the north) or HIPASS (in the south). Obscuration by Galactic H I eliminated about one half of the otherwise detectable objects. The total H I masses involved in these two model populations were $4.3 \times 10^9\ M_\odot$ and $6.4 \times 10^9\ M_\odot$, respectively. In both cases, about 75% of this mass had already been consumed by M 31 and the Galaxy via cloud disruption, leaving only 25% still in circulation, although distributed over some 1200 low–mass objects.

The crucial role of survey sensitivity in determining what is seen of such Local Group cloud populations is also illustrated in Figs. 21 and 22. The red symbols in these figures indicate objects detectable with the relevant LDS or HIPASS sensitivities, while the black symbols indicate those that remain undetected due to either limited sensitivity or obscuration. If these models describe the actual distribution of objects, then the prediction is that future deeper surveys will detect large numbers of objects at high negative LSR velocities in the general vicinity (about $60 \times 60°$) of M 31. To make this prediction more specific, we have imagined the sensitivity afforded by the cur-

Table 5. Model statistics for the best–fit Local Group models. The total numbers of objects and their H I masses are indicated for models #9 and #3 (see Table 4) together with how these are distributed within different categories. A detected sample of 163 objects was required in all cases after obscuration by the Galaxy and excluding the anomalous south Galactic pole region at $b, -65°$. The table also lists the number of objects classified as disrupted by ram–pressure or tidal stripping as well as those too faint to be detected by the LDS or HIPASS observations.

Fate of input CHVCs	model #9		model #3	
	number of CHVCs	$M_{\rm HI}$ ($10^8\ M_\odot$)	number of CHVCs	$M_{\rm HI}$ ($10^8\ M_\odot$)
Total number	6281	43	6310	64
Disrupted by ram or tide	4759	31	5178	50
Too faint to be detected	1220	6.5	831	4.4
Detectable if not obscured	302	5.4	301	10
Unobscured by H I ZoA	173	3.3	172	6.5
Unobscured, not at SGP	163	3.2	163	6.4

rent HIPASS survey in the south extended to the entire northern hemisphere. Figure 23 illustrates the prediction. A high concentration of about 250 faint newly detected CHVCs is predicted in the Local Group barycenter direction once HIPASS sensitivity is available.

5. A Galactic Halo population model for the CHVC ensemble

In the previous section we have outlined a physical model for self–gravitating, dark–matter dominated CHVCs evolving in the Local Group potential. While that model was quite successful in describing the global properties of the CHVC phenomenon, we noted that some aspects of the observed kinematic and spatial deployment were strongly influenced by the effects of obscuration by foreground Galactic H I and that, furthermore, the sensitivity limitations of the currently available H I survey material preclude tightly constraining the characteristic distances. In this section we consider to what extent a straightforward model in which the CHVCs are distributed throughout an extended halo centered on the Galaxy might also satisfy the observational constraints. We consider such a Galactic Halo model ad hoc in the sense that it lacks the physical motivation that the hierarchical structure paradigm affords the Local Group model.

We consider a spherically symmetric distribution of clouds, centered on the Galaxy. The radial density profile of the population is described by a Gaussian function, with its peak located at the Galactic center and its dispersion to be specified as a free parameter of the simulations. The H I mass distribution is given by a power–law, the slope of which is a free parameter. Different values are allowed for the lowest H I mass in the simulation. The H I density distribution of an individual cloud is also described by a Gaussian function. The central volume density is the same for all clouds in a particular simulation. Given the H I mass and central density of an object, the spatial *FWHM* of the H I distribution follows. For the velocity *FWHM* we have simply adopted the thermal linewdth of an 8000 K H I gas of 21 km s^{-1}.

Each simulated cloud is "observed" with the parameters corresponding to the LDS observations, if it is located in the northern celestial hemisphere, but with the HIPASS parameters if it is located in the southern hemisphere. Clouds are removed from the simulation if they are too faint to be detected. To include the effects of obscuration by the Milky Way, the velocity field of the clouds must be specified. The population is considered in the Galactic Standard of Rest system, where it is distributed as a Gaussian with a mean velocity of -50 km s^{-1} and dispersion of 110 km s^{-1}. These values follow directly from the observed parameters summarized in Table 2 after correction for obscuration as in Fig. 2. Clouds with a deviation velocity (as defined in Sect. 2.2.1) less than 70 km s^{-1} are removed. Additional clouds that pass the selection criteria are simulated until their number equals the number of CHVCs actually observed.

We performed the simulations with the following values for the four parameters that describe the distance, H I mass, and spatial extent of the population.

- The spatial dispersion of the cloud population. Values range from 10 kpc to 2 Mpc; specifically we consider the values of 10, 15, 20, ... 50, 60, 70, ... 100, 150, 200, ... 500, 1000, 2000 kpc;
- The slope of the H I mass distribution, β. Values for β were $-2.0, -1.8, \ldots, -0.8$;
- The lowest H I mass, M_0, allowed in a simulation. Values for M_0 were 10^2, 10^3, 10^4, or $10^5\ M_\odot$;
- The central gas density in the clouds, n_0. Values for n_0, which remained constant for a single run, were 3×10^{-3}, 1×10^{-2}, 3×10^{-2}, 0.1, and 0.3 cm^{-3}.

The only measured quantities which can usefully be compared to the models are the distributions of angular sizes and peak column densities. This is because the average kinematics in these simulations have already been defined to match the data by our choice of the mean velocity and its dispersion. Given four free model parameters for each simulation and only two distributions to determine the degree of agreement between simulations and observations, it is clear that the problem is under–determined. We can only hope to constrain the range

of reasonable parameters in the four–dimensional parameter space.

In order to assess the degree of agreement between the simulation outcomes and the observations, we use a χ^2–test from Sect. 14.3 of *Numerical Recipes*, (Press et al. 1993). The size and column density distributions of the models and the data are compared. A simulation was considered acceptable if $\chi^2(\text{size}) < 5$ and $\chi^2(N_{\rm HI}) < 5$. Figure 24 shows examples of the range of fit quality that was deemed acceptable for both the column density and size distributions.

Table 6 lists the parameter combinations that produce formally acceptable results, and shows that for each M_0 value the acceptable solutions are concentrated around a line. The solutions range from nearby models, for which the central density is of the order of 0.1 cm^{-3}, the mass slope is −2.0, and the characteristic distance is several tens of kpc, to more distant models, having a central density of 0.01 cm^{-3}, a mass slope of −1.4, and characteristic distances of several hundreds of kpc. Since column density is simply the product of depth and density this coupling of distance to central density is easily understood.

Overviews of two of the best–fitting models of the Galactic Halo type are given in Figs. 25 and 26. Figure 25 shows a cloud population with 30 kpc dispersion, while the population in Fig. 26 has a dispersion of 200 kpc. These figures can be compared with Fig. 9, showing the situation actually observed. Despite there being almost a factor of ten difference in the average object distance for these two models, they produce similar distributions of observables, which are to a large extent determined by the effects of obscuration. Relative to the observed CHVC sample shown in Fig. 9, the density distributions of these models are more uniformly distributed on the sky. The average velocity fields are also more symmetric about $b = 0°$, lacking the extreme negative excursion toward $(l, b) = (125°, -30°)$ seen in the CHVC population, that produces a large gradient in the $(V_{\rm GSR}, b)$ plot.

6. Discussion and conclusions

The effects of both obscuration by the gaseous disk of the Galaxy and the limited sensitivity of currently available H I surveys have important consequences for the observed properties of the HVC phenomenon. We have identified those consequences in this paper. Obscuration leads to apparent localized enhancements of object density, as well as to systematic kinematic trends that need not be inherent to the population of CHVCs. A varying resolution and sensitivity over the sky substantially complicates the interpretation of the observed distributions. Taking account of both these effects in a realistic manner is crucial to assessing the viability of models for the origin and deployment of the anomalous–velocity H I. Our discussion leads to specific predictions for the numbers and kinematics of faint CHVCs which can be tested in future H I surveys.

6.1. Galactic Halo models

As shown in Sect. 5, a straightforward empirical model in which CHVCs are dispersed throughout an extended halo centered on the Galaxy does not provide the means to discriminate between distances typical of the Galactic Halo and those of the Local Group. Comparable fit quality is realized for distance dispersions ranging from about 30 to 300 kpc. In addition to requiring a relatively large number of free parameters, such empirical models beg a number of serious physical questions. In the first instance: how is it that H I clouds can survive at all in a low–pressure, high–radiation–density environment without the pressure support given by a dark halo? Presumably such "naked" Galactic Halo H I clouds would either be very short–lived or require continuous replenishment, since the timescales for reaching thermal and pressure equilibrium are only about 10^7 years (Wolfire et al. 1995). Realistic assessment of such a scenario must await more detailed simulations that track the long–term fate of gas, for example after tidal stripping from the LMC/SMC, within the Galactic Halo. Only by including more physics will it be possible to reduce the number of free parameters and determine meaningful constraints on this type of scenario. This class of model also suffers from a number of shortcomings in describing the observed distributions, namely that the object density enhancement coupled with high negative velocities seen in the Local Group barycenter direction are not reproduced.

The Galactic Halo simulations returned formally acceptable values of characteristic distance as low as some 30 kpc. There is, however, a growing body of independent evidence based on high–resolution imaging of a limited number of individual CHVCs that such nearby distances do not apply. Braun & Burton (2000) discussed evidence from Westerbork synthesis observations of rotating cores in CHVC? 204.2 + 29.8 + 075 (using the de Heij et al. 2002 notation for a semi-isolated source) whose internal kinematics could be well modeled by rotation curves in flattened disk systems within cold dark matter halos as parameterized by Navarro et al. (1997), if at a distance of at least several hundred kpc. Similar distances were indicated for CHVC? 115.4 + 13.4 − 260 on the basis of dynamical stability and crossing–time arguments regarding the several cores observed with different systemic velocities, but embedded in a common diffuse envelope. The WSRT data for CHVC 125.3 + 41.3 − 205 likewise supported distances of several hundred kpc, based on a volume–density constraint stemming from the observed upper limit to the kinetic temperature of 85 K. Burton et al. (2001) found evidence in Arecibo imaging of ten CHVCs for exponential edge profiles of the individual objects: the outer envelopes of the CHVCs are not tidally truncated and thus are likely to lie at substantial distances from the Milky Way. For plausible values of the thermal pressure at the core/halo interface, these edge profiles support distance estimates which range between 150 and 850 kpc.

6.2. Local Group models

The Local Group deployment models of Sect. 4 offer a more self–consistent and physically motivated scenario for the CHVC population. Dark–matter halos provide the gravitational confinement needed to produce a two–phase atomic medium with cool H I condensations within warm H I envelopes, and provide in addition the necessary protection against ram–

Table 6. Results of the models described in Sect. 5, in which the CHVCs are viewed as forming an extended halo population, centered on the Galaxy. Each simulation is determined by four free parameters, namely the central H I density of the clouds, n_0, the slope of the H I mass distribution, β, the lowest H I mass in each simulation, M_0, and the dispersion of the spatial Gaussian that defines the distance, σ_d, of the cloud population. The simulations were sampled with the observational parameters of the LDS and HIPASS surveys and compared with the CHVC sample. The table shows which distance dispersions produce acceptable results for each of the combinations of n_0, β, and M_0. A field is blank if there is no good fit for the given parameter combinations. A simulation is considered successful if $\chi^2_{\rm size} < 5$ and $\chi^2_{N_{\rm HI}} < 5$. The central cloud density, n_0, is shown horizontally above each section of the table, in units cm^{-3}; the slope of the H I mass distribution is listed vertically on the left of the table: M_0 ranges from 10^2 $M_\odot$ for the top table to 10^5 $M_\odot$ for the bottom table. Distances are in kpc. The model is not tightly constrained, because of degeneracies in parameter combinations.

Simulations with $M_0 = 10^2$:

	$n_0 = 3 \times 10^{-3}$ cm^{-3}	1×10^{-2} cm^{-3}	3×10^{-2} cm^{-3}	1×10^{-1} cm^{-3}	3×10^{-1} cm^{-3}
$\beta = -1.0$					
−1.2	σ_d =150 … 300 kpc	35 … 45	10 … 20		
−1.4	200 … 350	45 … 100	15 … 40	15	
−1.6	200 … 350				
−1.8	500				
−2.0					

Simulations with $M_0 = 10^3$:

	$n_0 = 3 \times 10^{-3}$ cm^{-3}	1×10^{-2} cm^{-3}	3×10^{-2} cm^{-3}	1×10^{-1} cm^{-3}	3×10^{-1} cm^{-3}
$\beta = -1.0$					
−1.2		70 … 100			
−1.4	σ_d =100 … 400 kpc	45 … 100	15 … 40	15	
−1.6	200	50, 90	15 … 25	10 … 15	
−1.8			10 … 15	10 … 15	
−2.0			10	10 … 15	

Simulations with $M_0 = 10^4$:

	$n_0 = 3 \times 10^{-3}$ cm^{-3}	1×10^{-2} cm^{-3}	3×10^{-2} cm^{-3}	1×10^{-1} cm^{-3}	3×10^{-1} cm^{-3}
$\beta = -1.0$					
−1.2	σ_d =100 … 250 kpc				
−1.4	150 … 450	50 … 100	50 … 70		
−1.6	400	45 … 100	40 … 50		
−1.8		40 … 60	30 … 45		
−2.0		40 … 45	30 … 45		

Simulations with $M_0 = 10^5$:

	$n_0 = 3 \times 10^{-3}$ cm^{-3}	1×10^{-2} cm^{-3}	3×10^{-2} cm^{-3}	1×10^{-1} cm^{-3}	3×10^{-1} cm^{-3}
$\beta = -1.0$					
−1.2	σ_d = 250 kpc				
−1.4	250 … 450	150			
−1.6	150 … 300	100 … 150			
−1.8	150 … 200	100 … 150			
−2.0		90 … 150			

pressure and tidal stripping to allow long–term survival. The kinematics of the population follow directly from an assumed passive evolution within the Local Group potential. While three free parameters (the distance scalelength, the mass function slope, and the upper mass cut–off) were then tuned to explore consistency with the observations, only the distance was effectively a "free" parameter. The mass function slopes of the best fits have values of −1.7 to −1.8, in rough agreement with the value of −1.6 favored by Chiu et al. (2001) for the distribution of the baryonic masses in their cosmological simulations. The somewhat steeper slopes and therefore larger baryonic fractions favored by our model fits might be accomodated by recondensation onto the dark–matter halos at later times.

The H I upper mass cut–off introduced in the Local Group models can also be externally constrained. In addition to satisfying the observational demand that no H I column densities exceeding a few times 10^{20} cm^{-2} are seen in the CHVC population (consistent with the absence of current internal star formation), there is the observed lower limit of about $3{\times}10^7$ $M_\odot$ for the H I mass seen in a large sample of late–type dwarf galaxies (Swaters 1999). The upper mass cut–off favored by the simulations, of about 10^7 $M_\odot$, is essentially unavoidable given these two constraints.

The spatial Gaussian dispersion which is favored by these simulations is quite tightly constrained to lie between about 150 and 200 kpc. The implication for the distribution of ob-

ject distances is illustrated in Fig. 27 in the form of a histogram of the detected objects from model #9. The distribution has a broad peak extending from about 200 to 450 kpc with a few outliers extending out to 1 Mpc due primarily to the M 31 sub–population. The filled circles in the figure are the distance estimates for individual CHVCs found by Braun & Burton (2000) and Burton et al. (2001). Although very few in number, these estimates appear consistent with the model distribution, also peaking in number near 250 kpc.

We have made the simplifying assumption that the baryonic matter in our model clouds is exclusively in the form of H I, rather than being partially ionized. It is reassuring that the best-fitting models have peak column densities which are sufficiently high that the objects should be self-shielding to the extragalactic ionizing radiation field for $M_{\rm HI} > 10^{5.5}\,M_\odot$ as noted above. Since the neutral component requires a power–law slope of about −1.7 to fit the data, it seems likely that the total baryonic mass distribution might follow an even steeper distribution, since the mass fraction of ionized gas will increase toward lower masses.

6.3. The Local Group mass function

An interesting question to consider is whether the extrapolated mass distributions of our Local Group CHVC models can also account for the number of galaxies currently seen. In Fig. 28 we plot the mass distribution of objects in one of the best–fitting Local Group models, model #9 of Table 4. The thin–line histogram gives the mass distribution of the model population after accounting for the effects of ram–pressure and tidal stripping. The thick–line histogram gives the observed CHVC distribution that results from applying the effects of Galactic obscuration and sensitivity limitations appropriate to the LDS and HIPASS properties in the northern and southern hemispheres, respectively. The hatched histogram gives the inferred total baryonic (H I plus stellar) mass distribution of the Local Group galaxies tabulated by Mateo (1998), assuming a stellar mass–to–light ratio of $M/L_B = 3\,M_\odot/L_\odot$. M 31 and the Galaxy, with baryonic masses of some $10^{11}\,M_\odot$, are not included in the plot. The diagonal line in the figure has the slope of the model H I mass function of $\beta = -1.7$. The figure demonstrates that the low–mass populations of these models are roughly in keeping with what is expected from the number of massive galaxies together with a constant mass function slope of about $\beta = -1.7$. At intermediate masses, 10^7–$10^{8.5}\,M_\odot$, there is a small deficit of cataloged Local Group objects relative to this extrapolated distribution, while at higher masses there is a small excess. Conceivably this may be the result of galaxy evolution by mergers.

It is important to note that the distribution of objects shown in Fig. 28 is only the current relic of a much more extensive parent population. As shown in Table 5, about 75% of the CHVC population in these models is predicted to have been disrupted by ram pressure or tidal stripping over a Hubble time, contributing about $3 \times 10^9\,M_\odot$ of baryons to the Local Group environment and the major galaxies.

6.4. The M 31 population of CHVCs

One of the most suggestive attributes of the CHVC population in favor of a Local Group deployment is the modest concentration of objects which are currently detected in the general direction of M 31, i.e. in the direction of the Local Group barycenter. These objects have extreme negative velocities in the GSR reference frame. While this is a natural consequence of the Local Group models it does not follow from the empirical Galactic halo models, nor is it a consequence of obscuration by Galactic H I. Putman & Moore (2002) have made some comparisons between numerical simulations of dark matter mini–halos in the Local Group with the $(l, V_{\rm LGSR})$ distributions of HVCs and CHVCs, and were led to reject the possibility of CHVC deployment throughout the Local Group. Our discussion here has shown that such comparisons require taking explicit account of detection thresholds in the available survey observations, as well as of the vagaries of obscuration caused by the H I Zone of Avoidance. The Putman & Moore investigation did not take these matters into account. The modest apparent amplitude of the M 31 concentration relative to the Galactic population as seen with present survey sensitivities provides the best current constraints on the global distance scale of the CHVC ensemble. There follows a testable prediction, namely that with increased sensitivity a larger fraction of the M 31 population of CHVCs should be detected. This prediction was made explicit in Fig. 23, where one of our model distributions was shown as it would have been detected if HIPASS sensitivity were available in the northern sky. For that particular model, some 250 additional detected objects are predicted, of which the majority are concentrated in the 60×60° region centered on M 31. The ongoing HIJASS survey of the sky north of $\delta = 25°$ (Kilborn 2002), which is being carried out using the 76–m Lovell Telescope at Jodrell Bank to about the same velocity coverage, angular resolution, and sensitivity as the HIPASS effort, should allow this prediction to be tested.

6.5. The Sculptor Group lines of sight

We have omitted the part of the sky around the south Galactic pole in our fitting of Local Group models to the observations, because of the extreme velocity dispersions measured in this direction. The nearest external group of galaxies, the Sculptor Group, is located in the direction of the south Galactic pole. If the CHVCs are distributed around the major Local Group galaxies, then plausibly the same sort of objects could be present in the Sculptor Group. Putman et al. (2002) mention detection of clouds in the direction of the southern part of the Sculptor Group. Because no similar clouds were detected in the northern part of this Group, they consider it unlikely that this concentration of CHVCs is associated with the Sculptor Group. We note, however, that rather than being a spherical concentration of galaxies, the Sculptor Group has an extended filamentary morphology, which ranges in distance from 1.7 Mpc in the south to 4.4 Mpc in the north. Putman et al. assumed that the HIPASS sensitivity would allow detection of H I masses of $7 \times 10^6\,M_\odot$ throughout the Sculptor Group. But in Fig. 13 we show the actual distance out to which HIPASS

can detect H I masses given a realistic cloud model and detection threshold: even the most massive and rare objects in our simulated distributions, with $M_{\rm HI} = 10^7\ M_\odot$, can only be detected out to 2.5 Mpc. It is therefore only the near portion of the Sculptor filament that might be expected to show any enhancement in CHVC density with the currently available sensitivities.

6.6. Predicted CHVC populations in other galaxy groups

It is also interesting to consider whether the simulated Local Group model populations would be observable in external galaxy groups at even larger distances. In Fig. 29 we show one of our best–fitting Local Group models, model #9 of Table 4, projected onto a plane as in Fig. 20. In Fig. 20, the surviving clouds were distinguished by H I flux; in Fig. 29, the distinction is by H I mass. We indicate with grey dots those objects that were deemed to have been disrupted by ram–pressure or tidal stripping. The red and black dots indicate the remaining objects in the population, with the red dots representing objects that exceed $M_{\rm HI} = 3 \times 10^6\ M_\odot$ and the black dots those that fall below this mass limit. The choice of a limiting mass of $M_{\rm HI} = 3 \times 10^6\ M_\odot$ over a linewidth of 35 km s^{-1} was made to represent what might be possible for a deep H I survey of an external galaxy group. In this example, some 95 objects occur which exceed this mass limit distributed over a region of some 1.5×1.0 Mpc extent. For a limiting mass of $M_{\rm HI} = 5 \times 10^6\ M_\odot$ over 35 km s^{-1}, the number drops to 45. It is clear that a very good mass sensitivity will be essential to detecting such potential CHVC populations in external galaxy groups. Current searches for such populations, reviewed by Braun & Burton (2001), have generally not reached a sensitivity as good as even $M_{\rm HI} = 10^7\ M_\odot$ over 35 km s^{-1}, so it is no surprise that such distant CHVCs have not yet been detected.

Acknowledgements. The Westerbork Synthesis Radio Telescope is operated by the Netherlands Foundation for Research in Astronomy, under contract with the Netherlands Organization for Scientific Research.

References

Bajaja, E., Morras, R., & Pöppel, W. G. L. 1987, Pub. Astr. Inst. Czech. Ac. Sci., 69, 237
Barnes, D. G., Staveley–Smith, L., de Blok, W. J. G., et al. 2001, MNRAS, 322, 486
Blitz, L., Spergel, D. N., Teuben, P. J., Hartmann, D., & Burton, W. B. 1999, ApJ, 514, 818
Braun, R., & Burton, W. B. 1999, A&A, 341, 437
Braun, R., & Burton, W. B. 2000, A&A, 354, 853
Braun, R., & Burton, W. B. 2001, A&A, 375, 219
Burkert, A. 1995, ApJ, 447, L25
Bregman, J. N. 1980, ApJ, 236, 577
Burton, W. B., Braun, R., Walterbos, R. A. M. & Hoopes, C. G. 1999, AJ, 117, 194
Burton, W. B., Braun, R., & Chengalur, J. N. 2001, A&A, 369, 616, (erratum in A&A, 375, 227)
Chiu, W. A., Gnedin, N. Y., & Ostriker, J. P. 2001, ApJ, 563, 21
Choi, P. I., Guhathakurta, P., & Johnston, K. V. 2002, AJ, submitted; see also [astro-ph/0111465]
Corbelli, E., & Salpeter, E. E. 1993, ApJ, 419, 104
de Heij, V., Braun, R., & Burton, W. B. 2002, A&A, in press, [astro-ph/0201249] (Paper I)
Eichler, D. 1976, ApJ, 208, 694
Einasto, J., Haud, U., Jôeveer, M., & Kaasik, A. 1976, MNRAS, 177, 357
Giovanelli, R. 1981, AJ, 86, 1468
Hartmann, D., Kalberla, P. M. W., Burton, W. B., & Mebold, U. 1996, A&AS, 119, 115
Hartmann, D., & Burton, W. B. 1997, Atlas of Galactic Neutral Hydrogen (Cambridge University Press)
Helmi, A., White, S. D. M., de Zeeuw, P. T., & Zhao, H. S. 1999, Nature, 402, 53
Henning, P. A., Kraan-Korteweg, R. C., Rivers, A. J., et al. 1998, AJ, 115, 584
Henning, P. A., Staveley-Smith, L., Ekers, R. D., et al. 2000, AJ, 119, 2686
Hulsbosch, A. N. M. 1978, A&A, 66, L5
Ibata, R., Gilmore, G., & Irwin, M. 1994, Nature, 370, 194
Ibata, R., Irwin, M., Lewis, G., et al. 2001, Nature, 412, 49
Karachentsev, I. D., & Makarov, D. A. 1996, AJ, 111, 794
Juraszek, S. J., Staveley-Smith, L., Kraan-Korteweg, R. C., et al. 2000, AJ, 119, 1627
Kilborn, V. A. 2002, in Seeing through the Dust, ASP Conf. Ser., ed. R. Taylor, T. Landecker, & T. Willis, in press
Klypin, A., Kravtsov, A. V., Valenzuela, O., & Prada, F. 1999, ApJ, 522, 82
Kraan–Korteweg, R. C. 1986, A&AS, 66, 255
Majewski, S., Ostheimer, J. C., Patterson, R. J., et al. 2000, AJ, 119, 760
Maloney, P. 1993, ApJ, 414, 41
Mateo, M. L. 1998, ARA&A, 36, 435
Moore, B., Calcaneo–Roldan, C., Stadel, J., et al. 2001, Phys. Rev. D., 64, 3508 [astro-ph/0106271]
Moore, B., Ghigna, S., Governato, G., et al. 1999, ApJ, 524, L19
Muller, C. A., Oort, J. H., & Raimond, E. 1963, C. R. Acad. Sci. Paris 257, 1661
Navarro, J. F., Frenk, C. S., & White, S. D. M. 1997, ApJ, 490, 493
Oort, J. H. 1926, Ph.D. Thesis, University of Groningen
Oort, J. H. 1966, Bull. Astr. Inst. Netherlands, 18, 421
Oort, J. H. 1970, A&A, 7, 381
Oort, J. H. 1981, A&A, 94, 359
Pietz, J., Kerp, J., Kalberla, P. M. W., Burton, W. B., Hartmann, D., & Mebold, U. 1998, A&A, 332, 55
Press, W. H., Teukolsky, S. A., Vetterling, W. T., & Flannery, B. P. 1993, Numerical Recipes in C (Cambridge University Press)
Putman, M. E., & Gibson, B. K. 1999, PASA, 16, 70
Putman, M. E. 2000, Ph.D. Thesis, Australian National University
Putman, M. E., de Heij, V., Stavely–Smith, L., et al. 2002, AJ, 123, 873
Putman, M. E., & Moore, B. 2002, in Extragalactic Gas at Low Redshift, ASP Conf. Ser., ed. J. Mulchaey, & J. Stocke, in press [astro-ph/0110417]
Raychaudhury, S., & Lynden–Bell, D. 1989, MNRAS, 240, 115
Sandage, A. 1986, ApJ, 307, 1
Shapiro, P. R., & Field, G. B. 1976, ApJ, 205, 762
Swaters, R. A. 1999, Ph.D. Thesis, University of Groningen
van den Bergh, S. 1994, AJ, 107, 1328
van Woerden, H., Schwarz, U. J., Peletier, R. F., Wakker, B. P., & Kalberla, P. M. W. 1999, Nature, 400, 138
Verschuur, G. L. 1975, ARA&A, 13, 257

Voskes, T., & Burton, W. B. 1999, in ASP Conf. Ser. 168, New Perspectives on the Interstellar Medium, ed. A. R. Taylor, T. L. Landecker, & G. Joncas, 375
Wakker, B. P. 1990, Ph.D. Thesis, University of Groningen
Wakker, B. P. 2001, ApJS, 136, 463
Wakker, B. P., & van Woerden, H. 1991, A&A, 250, 509
Wakker, B. P., & van Woerden, H. 1997, ARA&A, 35, 217
Wolfire, M. G., McKee, C. F., Hollenbach, D., & Tielens, A. G. G. M. 1995, ApJ, 453, 673